

**Meereswissenschaftliche Berichte**  
**MARINE SCIENCE REPORTS**

No. 10

**Analytical Theory and Numerical  
Experiments to the Forcing of Flow at  
Isolated Topographic Features**

by

**Martin Schmidt**

**Institut für Ostseeforschung  
Warnemünde  
1995**

## Contents

<b>Abstract</b>	<b>3</b>
<b>1 Introduction</b>	<b>4</b>
<b>2 Analytical approximations</b>	<b>8</b>
2.1 The basic equations . . . . .	8
2.2 Boundary conditions . . . . .	11
2.3 Formal solution of the vorticity equation using a Green function	13
2.4 Calculation of the Green function for an unbounded ocean . . . .	15
2.5 Approximate solution for an isolated cylindrical seamount . . . .	17
2.5.1 The barotropic solution . . . . .	18
2.5.2 Baroclinic approximations . . . . .	34
<b>3 Comparison with a numerical model</b>	<b>40</b>
<b>4 Summary</b>	<b>49</b>
<b>A The approximation of weak stratification</b>	<b>51</b>
<b>B Exact solution of the barotropic equation</b>	<b>52</b>
<b>C The baroclinic approximation</b>	<b>53</b>
C.1 Solution by iteration . . . . .	56
C.2 Decomposition into vertical eigenfunctions . . . . .	58
<b>Acknowledgement</b>	<b>60</b>
<b>References</b>	<b>60</b>

## Abstract

Topographic Rossby waves trapped at a cylindrical seamount are studied under conditions where a linear theory applies. In the barotropic approximation an exact analytical solution valid for obstacles of arbitrary height is derived, baroclinic effects are included approximately. The frequency of the topographic waves is proportionally to the inertial frequency and the relative obstacle height. Stratification increases the wave frequency and restricts the vertical extend of the pressure perturbation.

For a homogeneous upstream flow starting at  $t = 0$  the pressure perturbation and the flow field are calculated. The pressure perturbation encircles the obstacle clockwise as a dipole like structure, the velocity field is approximately in geostrophic balance. Due to friction the pressure perturbation becomes stationary after some time in correspondence to a very small flow velocities over the top of the obstacle.

The analytical results are compared with the free surface GFDL-model. For barotropic conditions there is a quantitative agreement of analytical and numerical results. In the baroclinic case especially for small seamounts a difference is found between the analytically and numerically calculated spectrum. This can be traced back to the coupling of low and high order vertical modes which are not resolved by the finite model grid.

## Zusammenfassung

Die Anregung topographischer Rossby-Wellen an einem zylindrischen unterseeischen Berg wird analytisch und mit numerischen Experimenten für den Fall untersucht, daß eine linear Theorie anwendbar ist. Unter barotropen Bedingungen wird eine exakte analytische Lösung, gültig für Berge beliebiger Höhe, angegeben, barokline Effekte werden näherungsweise berücksichtigt. Die Frequenz der topographischen Wellen ist zur Trägheitsfrequenz und zur relativen Höhe des Berges proportional. Durch die Schichtung wird die topographische Frequenz vergrößert und die Druckstörung am Boden lokalisiert.

Für eine bei  $t = 0$  beginnende homogene Anströmung werden die Druckstörung und das Geschwindigkeitsfeld berechnet. Die Druckstörung umläuft den Berg im Uhrzeigersinn als dipolartige Struktur, das Geschwindigkeitsfeld ist näherungsweise geostrophisch balanciert. Durch Reibung stellt sich ein stationärer Zustand mit einer sehr kleinen Stromgeschwindigkeit über dem Berg ein.

Die analytische Theorie wird mit dem GFDL-Modell verglichen. Unter barotropen Bedingungen ist die quantitative Übereinstimmung zwischen beiden exzellent. Im baroklinen Fall gibt es Abweichungen im Spektrum. Diese können auf im numerischen Modell nicht aufgelöste vertikale Moden höherer Ordnung zurückgeführt werden, die durch die Bodenrandbedingung an den barotropen sowie an niedrige vertikale Moden gekoppelt sind.

## 1 Introduction

The condition of zero mass flux through the seafloor is a simple boundary conditions supplementing the hydrodynamic equations. However, it involves a complex interplay of earth rotation, nonlinearity, stratification and friction. So the relation between flow and bottom topography is one of the basic and challenging problems of geophysical fluid dynamics and has been an interesting topic of theoretical and experimental research over several decades.

Whereas slowly varying or stationary phenomena governed by the conservation of potential vorticity are of importance for the oceanic circulation, in marginal or semienclosed seas mesoscale and small scale phenomena of high variability can dominate. A well defined large scale and permanent circulation may be absent and the flow patterns may persist at the most for some inertial periods. Modelling those processes requires highly resolving models with growing demands for the quantitative accuracy. Thus, it is worth to test the correctness of commonly used numerical models concerning the interaction of flow with the bottom topography. Since field data of semienclosed seas are the result of a complex superposition of processes of different nature, a direct comparison with numerical results is difficult. Alternatively, the comparison of analytical theories with numerical experiments is possible. For that purpose an analytical theory with an sufficient accuracy is needed.

The aim of the present paper is to compare an analytical theory of baroclinic topographic Rossby waves with numerical results from the free surface version of the GFDL-model, KILLWORTH et al. (1989). We consider simplified conditions, i.e., a flat bottom ocean with only some isolated topographic features. One can assume that the gross properties of the flow are independent of the topography and controlled by some idealized forcing, e.g., a homogeneous and barotropic upstream flow or flows with well defined stratification and shear. In this case the influence of the isolated topographic feature can be well identified and studied separately. Although the additional flow stems from a different boundary condition, it is called usually "topographically forced".

As an example the interaction of homogeneous flow with a rightcylindrical obstacle is revisited. There is an important difference between topographic

Rossby waves trapped at obstacles or elongated topographic structures as ridges and coastlines respectively. The topography of an obstacle is periodic in the angular co-ordinate. This allows only for special wavenumbers and leads to a discrete frequency spectrum. The excitation of these barotropic and baroclinic topographic Rossby waves is studied in more detail. Although the Rossby waves can be described in the frame of linearized hydrodynamics, the wave propagation is limited by nonlinear effects which should be shortly reconsidered. Stationary or slowly varying flow phenomena near obstacles are determined by the conservation of potential vorticity and friction. Over isolated obstacles larger than a critical height areas enclosed by streamlines, so called Taylor columns can be formed. For a barotropic ocean Taylor columns over small obstacles have been studied by INGERSOLL (1969), the stratified problem has been considered by HOGG (1973), McCARTNEY (1975) and HUPPERT (1975). OU (1991) has given an analytical theory of stationary flow near a cylindrical obstacle which can be applied also to high seamounts. A detailed analysis of stationary phenomena near obstacles has been given by KOZLOV (1993).

Considering stationary states only the flow in the Taylor columns is not uniquely defined. INGERSOLL (1996) obtained an unique analytical solution by adding an infinitesimal viscosity. FENNEL and SCHMIDT (1991) investigated the time dependent stratified flow over a cylindrical obstacle in the framework of an analytical inviscid quasigeostrophic approach. Their approach permits to follow the evolution of the flow from a starting phase governed by topographic waves towards a phase where the waves are damped by vortex shedding and vortex-vortex interaction. Finally, a stationary regime is established characterized by two eddies, an anticyclonic eddy trapped over the obstacle, whereas a cyclonic one leaves the obstacle downstream. A Taylor column is formed over the obstacle if its height is larger than a critical value. Although the stationary state is equivalent with that given by HOGG (1973) the flow within the Taylor column appears as the final state of an adjustment process. DAVEY et. al. (1993) as well as THOMPSON (1993) used an alternative method based on Koslovs contour dynamics to follow the evolution of the flow field near an obstacle within a two layer system.

The above scenario outlines the frame of existence of localized topographic Rossby waves. After the upstream flow has started, waves evolve from the compression of vorticity lines at the gradients of the topography. These waves can spread only if other effects balancing the vorticity production are small, i.e. the time scale of vortex shedding by advection or of damping by friction must be larger than the wave period. In the barotropic limit the frequency of the topographic waves is determined by the fractional height  $\delta$  of the obstacle, HUTHNANCE (1974), JOHNSON (1984). Stratification increases the topographic frequency, FENNEL and SCHMIDT (1991). In the frictionless limit the topographic waves are stopped after some time by advective effects. Alternatively, if friction is taken into account and the advective time scale is large the topographic waves are damped. In this case a frictionally controlled stationary state is established. The flow over the obstacle becomes very small, so this phenomenon may be called a frictionally controlled Taylor column. For the barotropic case for small topography this solution has been found by HICKIE (1972), the baroclinic generalization for small obstacles has been given by FENNEL and SCHMIDT (1991).

Alternatively to analytical theories which are restricted to simplified conditions numerical models are capable for realistic investigations. The stratified quasigeostrophic model of HUPPERT and BRYAN (1985) and the barotropic quasigeostrophic model of VERRON and LE PROVOST (1985) show topographic waves, vortex shedding and vortex-vortex interaction. The influence of vertical and horizontal momentum exchange can be studied. Whereas the model of Huppert and Bryan is periodic, the model of Verron and Le Provost has open boundary conditions and may run into stationary states for long times.

JAMES (1980) considered the pressure "lift" and "drag" forces due to the interaction of a seamount with a homogeneous barotropic upstream flow. He compared model results based on a numerical solution of the barotropic vorticity equation with the "drag" forces calculated from Ingersolls approach. Varying friction and advection his model shows either Taylor columns controlled by advection or friction. In the initial phase of the model runs topographic waves can be observed.

Several numerical experiments with models based on the primitive equa-

tions have been published which show the importance of topographic waves. BECKMANN et al. (1993) and HAIDVOGEL et al. (1993) investigated the flow near a tall isolated seamount using a  $\sigma$ -coordinate model. Using a periodic, i.e. tidal, forcing the frequency of the topographic waves can be estimated from the resonant amplification of the trapped flow for varying stratification. The results are in good agreement with the estimates of BRINK (1989).

With a model based on the Cox code SHERWIN and DALE (1992) have investigated the frequency of topographic waves trapped at a cylindrical obstacle as a function of the obstacle height. They are confronted with model results depending on the grid spacing.

Recently, GJEVIK and MOE (1994) used a multilayer model to investigate the influence of an obstacle on the flow over the Norwegian shelf. A similar experiment but based on the Mellor-Blumberg model has been performed by SLØRDAL et al. (1994). The model is initialized with a geostrophically balanced longshelf current. Then an isolated seamount is "grown up" on the shelf. Topographically induced eddy formation and vortex shedding by a large horizontal advection velocity are studied.

In the present paper analytical results are compared quantitatively with results of the GFDL-model. In section 2.1 a general approach towards an analytical theory of topographic forcing is given. As in the earlier paper of FENNEL and SCHMIDT (1991) a Green function method is used. The theory is developed further towards an applicability for finite height topography including the extreme case of flow near islands. The study is confined to a linear theory. It is sufficient to describe the excitation of topographic waves but its validity is restricted by the time scale of advection. Therefore, the damping of topographic waves due to advection as well as the formation of Taylor columns is beyond the present approach. Alternatively to a steady state determined by the balance of advection and Coriolis force a frictionally governed steady state may be established. In the present paper we will confine ourselves to small horizontal scales and use the  $f$ -plane approximation.

In section 2.5 the results are applied to the case of a cylindrical obstacle within a starting homogeneous flow. The topographic frequency as well as flow patterns are calculated for various values of the relative topographic height and

the stratification parameter.

In section 3 analytical results are compared with the results of numerical experiments with a free surface version of the GFDL-model, KILLWORTH et al. (1989). This model is based on the nonlinear, hydrostatic Boussinesq equations implemented as a finite difference scheme on an Arakawa B-grid. The comparison with the analytical results is not straightforward. The model geometry can be prepared with the same idealized conditions as in the analytical theory. However, numerical requirements restrict the range of physical parameters under investigation. Especially frictionless conditions cannot be established since friction is an essential ingredient to keep the model stable. The extraction of special quantities of interest is more difficult than from an analytical model. Also the resolution in space and time is limited by the conditions of numerical stability. Additional numerical difficulties, as a zero group velocity phenomenon in the Arakawa B-grid may influence the results, MESINGER and ARAKAWA (1976). The topographic frequency appears as suitable to compare analytical and numerical results also on a quantitative level.

## 2 Analytical approximations

### 2.1 The basic equations

We consider an unbounded, stratified, rotating and flat bottom ocean with an isolated topographic feature placed in the center of the co-ordinate system. We are interested in the starting flow problem, i.e. a homogeneous upstream flow  $u^0(t)$  is switched on at  $t = 0$  and we ask for the flow pattern emerging near the topographic feature. In this section analytically solvable approximations of the primitive equations are derived. For some physical processes very simple mathematical approximation are necessary. We restrict ourselves to timescales shorter than the advection time  $T_a$ , which can be defined as that time a water particle needs to be moved over a distance of the horizontal extension of the topographic feature  $A$ , i.e.,

$$A = \int_0^{T_a} dt u^0(t). \quad (2.1)$$

Then we can expect the linearized Boussinesq equations apply to a good approximation, i.e.,

$$u_t - fv + p_x = X, \quad (2.2)$$

$$v_t + fu + p_y = Y, \quad (2.3)$$

$$-b + p_z = 0, \quad (2.4)$$

$$b_t + N^2 w = Q. \quad (2.5)$$

Eq.s (2.4) and (2.5) can be combined to give

$$p_{zt} + N^2 w = Q. \quad (2.6)$$

The system is completed by the continuity equation for an incompressible fluid

$$u_x + v_y + w_z = 0. \quad (2.7)$$

Here  $u$  and  $v$  are the zonal and the meridional horizontal velocity components,  $w$  is the vertical velocity,  $p$  stands for the pressure deviation from the state of rest,  $b$  is the buoyancy and  $N^2$  is the Brunt Väisälä frequency. The subscripts  $x$ ,  $y$ ,  $z$  and  $t$  stand for the partial differentiation. Otherwise the notation is standard.

$f$  describes the horizontal component of the earth rotation, here we consider the  $f$ -plane approximation.  $x$ ,  $y$  and  $z$  orient to build a right handed system of kartesian co-ordinates.

The elevation of the free surface is related to the pressure at  $z = 0$

$$\eta = \frac{p}{g} \quad \text{at } z = 0. \quad (2.8)$$

The quantities  $X$ ,  $Y$  and  $Q$  symbolize the Reynolds stress, i.e., wind stress as an external force and internal Reynolds stress. For the sake of simplicity we consider a linear superposition of wind stress and internal Reynolds stress

$$(X, Y) = (X^w, Y^w) + (X^i, Y^i), \quad (2.9)$$

where the superscripts stand for  $^w$ : wind and  $^i$ : internal Reynolds stress. Wind forcing can be parameterized as a body force acting within a mixed layer of thickness  $H_{mix}$

$$(X^w, Y^w) = (\tau_x^w, \tau_y^w) \frac{\theta(z + H_{mix}^w)}{H_{mix}^w}. \quad (2.10)$$

$\tau^w$  is the wind stress at the surface. Bottom friction may be included by a similar layer, however, the calculations for finite topography will be complicated. For the internal Reynolds stress a simple ansatz

$$(X^i, Y^i) = -\nu(u, v) \quad (2.11)$$

is suitable for analytical investigations. The parameterization (2.11) implies a loss of momentum of the vertically integrated flow and we neglect additional bottom friction. Similarly we set

$$Q = -\nu b. \quad (2.12)$$

Diffusion vanishes for zero buoyancy, i.e. the stratification described by the Brunt Väisälä frequency  $N^2$  is a steady reference state. For simplicity the value of both the diffusion parameter for momentum and buoyancy have the same value.

The parameterization of turbulent processes as given above is simplified as much as possible. For a detailed discussion of turbulent processes in terms of a stationary quasigeostrophic boundary layer theory we refer to FOSTER (1989).

It is convenient to consider the Fourier transforms about  $t$ ,

$$A(t) = \int_{-\infty}^{+\infty} \frac{d\omega}{2\pi} e^{-i\omega t} A(\omega). \quad (2.13)$$

The quantities in the time- and the frequency domain are denoted by the same symbols and can be distinguished by their arguments.

It is not in the scope of this approach how the upstream flow  $u^0$  is driven. We assume there is some forcing which would produce a homogeneous flow in a flat bottom ocean, i.e. the flow field and the corresponding pressure are solutions of the Boussinesq equations for a flat bottom ocean. This flow is not necessarily in geostrophic balance. We subdivide all flow fields into an upstream part and a perturbation produced at the irregularities of the bottom topography,

$$\begin{aligned} \mathbf{u} &= \mathbf{u}^0 + \tilde{\mathbf{u}}, \\ p &= p^0 + \psi. \end{aligned} \quad (2.14)$$

Then, the topographically forced flow is a solution of the Boussinesq system

$$-i\bar{\omega}\tilde{u} - f\tilde{v} + \psi_x = 0, \quad (2.15)$$

$$-i\bar{\omega}\tilde{v} + f\tilde{u} + \psi_y = 0, \quad (2.16)$$

the equation of continuity

$$\tilde{u}_x + \tilde{v}_y + \tilde{w}_z = 0. \quad (2.17)$$

and the vertical equation

$$-i\bar{\omega}\psi_z + N^2\tilde{w} = 0. \quad (2.18)$$

The complex frequency  $\bar{\omega}$ ,

$$\bar{\omega} = \omega + i\nu, \quad (2.19)$$

emerges from the combination of the time derivative and the damping according to eq. (2.11).

This set of equations can be combined to one single equation for the pressure perturbation  $\psi$

$$-i\bar{\omega}(\Delta + \mathcal{Z})\psi(xyz\omega) = 0. \quad (2.20)$$

The operator  $\mathcal{Z}$  stands for

$$\mathcal{Z} = \frac{\partial}{\partial z} \frac{f^2 - \bar{\omega}^2}{N^2} \frac{\partial}{\partial z}. \quad (2.21)$$

## 2.2 Boundary conditions

We have to specify the boundary conditions for  $\psi$ .

At the surface we will assume the absence of horizontal air pressure gradients. Thus, in the linear approximation the vertical velocity at the surface equals the time derivative of the surface elevation  $\tilde{\eta}$

$$\tilde{w} = \tilde{\eta}_t \quad \text{for } z = 0. \quad (2.22)$$

or equivalently with eq.s (2.8) and (2.18) in the Fourier space

$$i\bar{\omega} \left( \psi_z + \frac{N^2}{g} \psi \right) = 0 \quad \text{for } z = 0. \quad (2.23)$$

In eq. (2.23) a small frictional term has been added to the time derivative of the free surface. This is convenient in the analysis below. Since the time scale of changes in the surface elevation is very short compared with the diffusive

time scale and the resulting error will be small. This minor inconsistency vanishes in the rigid lid approximation ( $w = 0$  at  $z = 0$ ).

At rigid boundaries, i.e. at the bottom and at the coast the flow perpendicular to the boundary vanishes

$$w = -\mathbf{u} \cdot \nabla H(xy) \quad \text{for } z = -H(xy). \quad (2.24)$$

The function  $H(xy) = H_0 - h(xy)$  describes the shape of the sea floor.

In the flat bottom case the vertical flow at the position  $z = -H(xy)$  is  $w^0$ . The vertical flow appearing additionally to  $w^0$  due to the influence of the bottom slope is

$$\tilde{w} = -w^0 - \mathbf{u} \cdot \nabla H(xy) \quad \text{for } z = -H(xy). \quad (2.25)$$

Subsequently, a nondivergent upstream flow is considered and  $w^0$  is zero.

Equations (2.25) includes the flat bottom,  $w = 0$ , and a sidewall like coast as special cases. In the latter case the normal derivative of  $H$  becomes infinitely large and one gets the usual coastal boundary condition of vanishing normal velocity,

$$\mathbf{u}_n = 0. \quad (2.26)$$

The horizontal equations

$$\tilde{u} = \frac{i\bar{\omega}\psi_x - f\psi_y}{f^2 - \bar{\omega}^2}, \quad (2.27)$$

$$\tilde{v} = \frac{i\bar{\omega}\psi_y + f\psi_x}{f^2 - \bar{\omega}^2}, \quad (2.28)$$

as well as eq. (2.18) can be used to eliminate the velocities,

$$\begin{aligned} (f^2 - \bar{\omega}^2) \left( \frac{i\bar{\omega}}{N^2} \psi_z + \mathbf{u}^0 \cdot \nabla H \right) \\ = -i\bar{\omega}(\nabla\psi) \cdot \nabla H - f((\nabla\psi) \times \nabla H)_z \quad \text{for } z = -H(xy). \end{aligned} \quad (2.29)$$

For a cylindrical obstacle with steep sidewalls and a flat top  $H$  reads in cylindrical co-ordinates

$$H(r, \varphi) = H_0 - h\theta(a - r), \quad (2.30)$$

and the above condition simplifies to

$$\begin{aligned} (f^2 - \bar{\omega}^2) \frac{i\bar{\omega}}{N^2} \psi_z &= 0, \quad \text{for } r \neq a \quad \text{and} \quad z = -H(r) \\ (f^2 - \bar{\omega}^2) u^0 \cos \varphi &= -i\bar{\omega} \psi_r + \frac{f}{r} \psi_\varphi \\ &\text{for } r = a \quad \text{and} \quad -H_0 < z < -H_0 + h. \end{aligned} \quad (2.31)$$

Considering localized processes as trapped topographic waves the pressure perturbation as well as its derivative should vanish far from the topographic feature

$$\begin{aligned} \psi &= 0 \quad \text{for } r \rightarrow \infty, \\ \psi_r &= 0 \quad \text{for } r \rightarrow \infty. \end{aligned} \quad (2.32)$$

For waves leaving the topographic feature an radiation condition applies.

### 2.3 Formal solution of the vorticity equation using a Green function

To discuss the properties of the solution of eq. (2.20) a formal solution is desirable. For linear differential equations as used here this can be accomplished by a Green function. Let us define a function  $G(xyzt, x'y'z't')$  governed by the equation (in frequency representation)

$$-i\bar{\omega} \Delta'_3 G(xyz, x'y'z', \omega) = \delta(x - x') \delta(y - y') \delta(z - z'). \quad (2.33)$$

Here, the primed derivatives act on the primed variables. For shorter notation the abbreviation

$$\Delta'_3 = \Delta' + \mathcal{Z}'. \quad (2.34)$$

has been introduced.

Next, we multiply eq. (2.33) by  $\psi$  and eq. (2.20) with  $G$ , add both equations and integrate over the total volume in the primed variables. In cylindrical co-ordinates  $r$ ,  $\varphi$  and  $z$

$$r = \sqrt{x^2 + y^2}, \quad (2.35)$$

$$\varphi = \arctan \left( \frac{y}{x} \right), \quad (2.36)$$

$$z = z, \quad (2.37)$$

we obtain

$$\psi(r\varphi z\omega) = \int_V dV' i\bar{\omega} (G\Delta'_3\psi - \psi\Delta'_3G). \quad (2.38)$$

The arguments of the functions under the integral have been omitted.

The usual procedure according the classical Green function method would be an integration by parts using Gauss' lemma or equivalently Green theorem. Choosing appropriate boundary conditions for the Green function the pressure would be given in the form of a convolution integral of the Green function with the sources of pressure perturbations, here the Reynolds stress term. However, this will be of no practical use because the Green function for a non flat bottom can be determined analytically only in some exceptional cases.

Alternatively, one can use a simplified Green function which fulfills simple boundary conditions and can be calculated analytically. In this case the Green function is not the "solving kernel". Additionally to the forcing term there appear further sources of pressure perturbations in connection with gradients of the bottom topography. Unfortunately these source terms depend on the pressure field itself, so the resulting equation has the form of an integral equation for the pressure, which, however, is only a two dimensional one.

Let us consider the Green function to be known. At the surface we require for the Green function the boundary condition

$$\frac{\partial G}{\partial z'} + \frac{N^2}{g}G = 0 \quad \text{for } z' = 0. \quad (2.39)$$

and at the bottom the boundary condition for the flat bottom case

$$\frac{\partial}{\partial z'}G = 0 \quad \text{for } z' = -H_0. \quad (2.40)$$

Eq. (2.38) can be integrated by parts. Using the bottom boundary condition (2.31) it follows

$$\begin{aligned} \psi(r\varphi z, \omega) = & \int_0^a dr' r' \int_0^{2\pi} d\varphi' i\bar{\omega} \frac{(f^2 - \bar{\omega}^2)}{N^2} \psi G_{z'} \Big|_{z'=-H_0+h} \\ & + \int_0^{2\pi} d\varphi' \int_{-H_0}^{-H_0+h} dz' \left( (f^2 - \bar{\omega}^2) Gu^0 a \cos \varphi' + i\bar{\omega} a \psi G_{r'} - fG\psi_{\varphi'} \right)_{r'=a}. \end{aligned} \quad (2.41)$$

This integro-differential equation can be solved numerically. The upstream flow appears as the forcing inhomogeneity. As an advantage compared to

the pressure equation it is only two dimensional and fulfills the boundary conditions automatically.  $\psi$  vanishes in the flat bottom case.

## 2.4 Calculation of the Green function for an unbounded ocean

We consider the Green function for an unbounded  $f$ -plane ocean with flat bottom as a reference state. We can decompose equation (2.33) for the Green function in vertical eigenfunctions  $F_n(z)$

$$G(\mathbf{r}z\mathbf{r}'z', \omega) = \sum_n F_n(z)F_n(z')G_n(\mathbf{r}\mathbf{r}', \omega). \quad (2.42)$$

The eigenfunctions are governed by the eigenvalue equation

$$\frac{\partial}{\partial z} \frac{1}{N^2} \frac{\partial}{\partial z} F_n(z) + \lambda_n^2 F_n(z) = 0. \quad (2.43)$$

The quantities  $\lambda_n$  are the eigenvalues corresponding to the  $F_n$ 's and are related to the Rossby radius as

$$R_n = (\lambda_n f)^{-1}. \quad (2.44)$$

The boundary conditions correspond to the kinematic boundary conditions for the pressure and the Green function, i.e.,

$$\frac{\partial F_n}{\partial z} + \frac{N^2}{g} F_n = 0 \quad \text{for } z = 0, \quad (2.45)$$

$$\frac{\partial F_n}{\partial z} = 0 \quad \text{for } z = -H_0. \quad (2.46)$$

The eigenfunctions are orthonormalized according to

$$\int_{-H_0}^0 dz F_n(z)F_m(z) = \delta_{nm} \quad (2.47)$$

and form a complete basis

$$\sum_{n=0}^{\infty} F_n(z)F_n(z') = \delta(z - z'). \quad (2.48)$$

$G_n$  is governed by the partial differential equation

$$-i\bar{\omega} (\Delta' + \kappa_n^2) G_n(\mathbf{r}\mathbf{r}'\omega) = \delta(\mathbf{r} - \mathbf{r}'), \quad (2.49)$$

where the abbreviation  $\kappa_n^2$  stands for

$$\kappa_n^2 = \lambda_n^2 (\bar{\omega}^2 - f^2). \quad (2.50)$$

The solution of eq. (2.49) is a Hankel function  $H_0^{(1)}$ , e.g. ARFKEN (1970) :

$$G_n(\mathbf{r}\mathbf{r}'\omega) = \frac{1}{4\bar{\omega}} H_0^{(1)}(|\mathbf{r} - \mathbf{r}'|\kappa_n). \quad (2.51)$$

It fulfills a radiation condition for large  $r'$  assuming  $\kappa_n$  is that root of  $\kappa_n^2$  with the positive imaginary part. In the case  $\omega < f$  the Hankel function may be transformed into a modified Bessel function  $K_0$  and  $G_n$  reads

$$G_n(\mathbf{r}\mathbf{r}'\omega) = \frac{1}{2\pi i \bar{\omega}} K_0(|\mathbf{r} - \mathbf{r}'|\alpha_n), \quad (2.52)$$

whereby,

$$\alpha_n^2 = -\kappa_n^2. \quad (2.53)$$

For later reference we note the Fourier series of  $G$  about the angular variable  $\varphi$

$$G(\mathbf{r}z\mathbf{r}'z', \omega) = \frac{i}{\bar{\omega}} \sum_{m=-\infty}^{m=\infty} \frac{e^{im(\varphi-\varphi')}}{2\pi} L_m(rzr'z'\omega), \quad (2.54)$$

with

$$L_m(rzr'z'\omega) = -\sum_n F_n(z)F_n(z')g_{mn}(rr'\omega). \quad (2.55)$$

The function  $g_{mn}$  reads

$$g_{mn}(r, r') = \theta(r - r')g_{mn}^>(r, r') + \theta(r' - r)g_{mn}^<(r, r'), \quad (2.56)$$

with

$$\begin{aligned} g_{mn}^>(r, r') &= K_m(r\alpha_n)I_m(r'\alpha_n), \\ g_{mn}^<(r, r') &= K_m(r'\alpha_n)I_m(r\alpha_n), \end{aligned} \quad (2.57)$$

or equivalently

$$\begin{aligned} g_{mn}^>(r, r') &= \frac{\pi i}{2} H_m^{(1)}(r\kappa_n)J_m(r'\kappa_n), \\ g_{mn}^<(r, r') &= \frac{\pi i}{2} H_m^{(1)}(r'\kappa_n)J_m(r\kappa_n). \end{aligned} \quad (2.58)$$

The former expression for  $g_{mn}$  has real arguments for  $|\omega| < f$ , whereas the second one is more appropriate for  $|\omega| > f$ . From the properties of  $K_m$  and  $I_m$  or  $H_m^{(1)}$  and  $J_m$  respectively, ABRAMOWITZ & STEGUN (1984), it follows

$$g_{mn} = g_{-mn}. \quad (2.59)$$

## 2.5 Approximate solution for an isolated cylindrical seamount

In this section eq. (2.41) will be solved approximately. In comparison with other results which confine to a topography of small height, the approach is applicable also to a topography with finite height including the island case. Mathematical details are given in the appendix. We start with the barotropic approximation. Here, an exact solution can be found. Baroclinic effects will be included approximately.

Because of the cylindrical symmetry of the topography, eq. (2.41) can be simplified by separation of the angular variable  $\varphi$ ,

$$\psi(r\varphi z\omega) = \sum_m \frac{e^{im\varphi}}{2\pi} \psi_m(rz\omega). \quad (2.60)$$

Assuming a homogeneous upstream flow  $u^0$  the remaining integral equation for the components  $\psi_m$  reads

$$\begin{aligned} \psi_m(rz\omega) = & - \int_0^a dr' r' \psi_m(r'z'\omega) \frac{f^2 - \bar{\omega}^2}{N^2} \frac{\partial}{\partial z'} L_m(rzr'z'\omega) \Big|_{z'=-H_0+h} \\ & + \int_{-H_0}^{-H_0+h} dz' i \frac{f^2 - \bar{\omega}^2}{\omega} u^0 \pi a \delta_{|m|,1} L_m(rzaz'\omega) \\ & + \int_{-H_0}^{-H_0+h} dz' \psi_m(az'\omega) \mathcal{G}_m(rzaz'\omega). \end{aligned} \quad (2.61)$$

We have used the abbreviation

$$\mathcal{G}_m(rzr'z'\omega) = -r' \frac{\partial}{\partial a} L_m(rzr'z'\omega) + \frac{fm}{\bar{\omega}} L_m(rzaz'\omega). \quad (2.62)$$

An explicit expression for  $\mathcal{G}_m$  is

$$\mathcal{G}_m(rzr'z'\omega) = \sum_n F_n(z) F_n(z') \mathcal{G}_{mn}(rr'\omega), \quad (2.63)$$

$$\mathcal{G}_{mn}(rr'\omega) = \theta(r-r') \mathcal{G}_{mn}^>(rr'\omega) + \theta(r'-r) \mathcal{G}_{mn}^<(rr'\omega) \quad (2.64)$$

with

$$\begin{aligned} \mathcal{G}_{mn}^>(rr'\omega) &= K_m(r\alpha_n) \left( r'\alpha_n I_{m+1}(r'\alpha_n) + m \left( 1 - \frac{f}{\bar{\omega}} \right) I_m(r'\alpha_n) \right), \\ \mathcal{G}_{mn}^<(rr'\omega) &= I_m(r\alpha_n) \left( -r'\alpha_n K_{m+1}(r'\alpha_n) + m \left( 1 - \frac{f}{\bar{\omega}} \right) K_m(r'\alpha_n) \right). \end{aligned} \quad (2.65)$$

$\mathcal{G}_{mn}$  has the important property

$$\mathcal{G}_{mn}^>(aaw) - \mathcal{G}_{mn}^<(aaw) = 1. \quad (2.66)$$

### 2.5.1 The barotropic solution

As a first example we consider the barotropic approximation. It follows from eq. (2.61) in the limit  $N^2 \rightarrow 0$ . The baroclinic components of the Green function are proportionally to the baroclinic Rossby radius  $R_1$  and vanish in the limit  $N^2 \rightarrow 0$ . For the derivatives of the Bessel functions in  $\mathcal{G}_m$  the limit  $N^2 \rightarrow 0$  must be performed before setting eventually  $r = a$ . The baroclinic part of the first contribution of eq. (2.61) does not become zero in the limit  $N^2 \rightarrow 0$  because the bottom geometry is expressed also in terms of the eigenfunctions  $F_n$ . The details are given in Appendix A.

Since the flow is independent of the depth  $z$  the barotropic equations are valid rather for the vertically integrated velocity (transport) than for the velocity itself. The number of degrees of freedom in the linear barotropic approximation is too small to adjust the velocity field to the shape of the topography. As a consequence the boundary conditions (2.31) have to be replaced by the weaker condition of a continuous transport perpendicular to the gradient of the topography. This happens automatically if the barotropic limit is carried out in eq. (2.61). For a cylindrical obstacle this boundary condition reads in terms of the radial velocity component at the obstacle edge

$$u^{ar}(a)H_0 = u^{ir}(a)(H_0 - h). \quad (2.67)$$

$u^{(a,i)r}$  is the velocity outside and over the obstacle.

The barotropic solution for the pressure perturbation forced at a cylindrical obstacle can be calculated exactly. The details are given in Appendix B. The resulting pressure perturbation over the obstacle  $\psi^i$  and beside the obstacle  $\psi^a$  reads

$$\psi_{m0}^a(r\omega) = \frac{-\frac{h}{H_0}C_u K_m(\alpha_0 r) I_m(\beta a) D_{m0}^{-1}}{\sigma_{m0}(\omega)}, \quad (2.68)$$

$$\psi_{m0}^i(r\omega) = \frac{-\frac{h}{H_0}C_u K_m(\alpha_0 a) I_m(\beta r) D_{m0}^{-1}}{\sigma_{m0}(\omega)}. \quad (2.69)$$

with

$$C_u = i \frac{f^2 - \bar{\omega}^2}{\bar{\omega}} u^0 \pi a \delta_{|m|,1}, \quad (2.70)$$

$$D_{m0} = a\beta I_{|m|+1}(\beta a) K_m(\alpha_0 a) + a\alpha_0 I_m(\beta a) K_{|m|+1}(\alpha_0 a), \quad (2.71)$$

$$\beta^2 = \tilde{\beta}^2 \alpha_0^2, \quad \tilde{\beta}^2 = \frac{H_0}{H_0 - h}, \quad (2.72)$$

and

$$\begin{aligned} \sigma_{m0}(\omega) = 1 - \frac{h}{H_0} - \frac{h}{H_0} \left( -a\alpha_0 K_{m+1}(\alpha_0 a) \right. \\ \left. + m \left( 1 - \frac{f}{\bar{\omega}} \right) K_m(\alpha_0 a) \right) I_m(\beta a) D_{m0}^{-1}. \end{aligned} \quad (2.73)$$

The eq.s (2.68) and (2.69) are valid for obstacles with arbitrary height  $h$  including the island case,  $h = H_0$ . The results as given above are very similarly to the findings of HUTHNANCE (1974) for topographic wave excited by tides at Rockall Bank. However, the tidal forcing couples the modes with  $m = \pm 1$  to the  $m = 0$  mode so that an additional contribution appears in his solution and the wave spectrum is different.

The frequency spectrum of the pressure perturbation  $\psi$  corresponds to the singularities of eq.s (2.68) and (2.69) respectively. It consists of a continuous part in the superinertial frequency range

$$f < |\bar{\omega}| < \infty, \quad (2.74)$$

and a discrete part at frequencies  $\omega_{m0}$  in the subinertial domain

$$-f < \bar{\omega} < f. \quad (2.75)$$

For the continuous spectrum,  $|\bar{\omega}| > f$ , the modified Bessel functions  $I_m$  and  $K_m$  can be rewritten as oscillating Bessel functions  $H_m^{(1)}$  and  $J_m$ .  $\psi$  describes the radiation of inertial waves which decay asymptotically as  $\sqrt{r}^{-1}$ . In the frequency domain  $-f < \bar{\omega} < f$  the modified Bessel function  $K_m$  decreases exponentially for large  $r$  and  $\psi$  describes waves trapped at the obstacle.

The discrete frequencies  $\bar{\omega}_{m0}$  are determined by the zeros of the denominator of eq.s (2.68) and (2.69),

$$\sigma_{m0}(\omega) = 0. \quad (2.76)$$

We can restrict the discussion to positive values of the angular mode number  $m$ , the case of negative  $m$  can be treated with the relation

$$\sigma_{-m0}(\omega) = \sigma_{m0}(-\omega). \quad (2.77)$$

For the spectrum the damping  $\nu$  is of minor importance, since  $\sigma_{m0}$  depends on  $\bar{\omega}$  only. The corresponding complex frequency values accounting for the damping explicitly can be calculated by

$$\omega_m = \bar{\omega}_m - i\nu. \quad (2.78)$$

We start the discussion with the island case. In the limit  $h \rightarrow H_0$  we obtain

$$\psi_{m0}^a(r\omega) = \frac{-C_u K_m(\alpha_0 r) I_m(\alpha_0 a)}{S_{m0}(\omega)}, \quad (2.79)$$

$$\psi_{m0}^i(r\omega) = 0. \quad (2.80)$$

(The latter equation is valid with the exception of the point  $r = a$ .)  $S_{m0}$  is the remainder of  $\sigma_{m0}$  in the island case. To find the discrete spectrum, i.e. the trapped waves, we have to solve the equation

$$S_{m0}(\omega) = \left( \alpha_0 K_{m+1}(a\alpha_0) - m \left( 1 - \frac{f}{\bar{\omega}} \right) K_m(a\alpha_0) \right) I_m(a\alpha_0) = 0. \quad (2.81)$$

The factor  $I_m(a\alpha_0)$  has been introduced for convenience and does not influence the spectrum.

The zero at  $\bar{\omega} = -\text{sig}(\hat{m})f$  corresponds to a free wave. There is at least one additional zero  $|\bar{\omega}_{m0}| < f$ . For positive values of  $m$  it follows  $\bar{\omega}_{mn} < 0$ . According to eq. (2.77) every solution  $\bar{\omega}_{mn}$  for positive  $m$  has a complementary solution  $-\bar{\omega}_{mn}$  for negative  $m$ .

A criterion for the existence of this second zero can be derived considering the slope of  $S_m$  in the point  $\bar{\omega} = -\text{sig}(m)f$ . There is a critical radius  $a_{m0}^{\text{crit}}$  for the trapping of waves at a cylindrical island, LONGUET-HIGGINS (1969),

$$a_{m0}^{\text{crit}} = \sqrt{|m|(|m| - 1)} R_0. \quad (2.82)$$

For  $a > a_{m0}^{\text{crit}}$  trapped waves can exist but not for  $a < a_{m0}^{\text{crit}}$ . Obviously, for the island case all vertical modes separate and the above result can be generalized for the baroclinic modes

$$a_{mn}^{\text{crit}} = \sqrt{|m|(|m| - 1)} R_n. \quad (2.83)$$

Often one has the situation that  $R_1 \ll a \ll R_0$  so the barotropic mode is untrapped, whereas near the island trapped baroclinic modes may exist. If  $a \gg a_{mn}^{\text{crit}}$  a rough estimate for  $\bar{\omega}_{mn}$  reads

$$\bar{\omega}_{mn} \approx -f \frac{R_n m}{a}. \quad (2.84)$$

This frequency belongs to waves with phases

$$\Phi \approx m \left( \varphi + f \frac{R_n}{a} t \right), \quad (2.85)$$

i.e. a Kelvin like wave with a wavenumber

$$k_\varphi = -\frac{m}{a} \quad (2.86)$$

encircling the island clockwise.

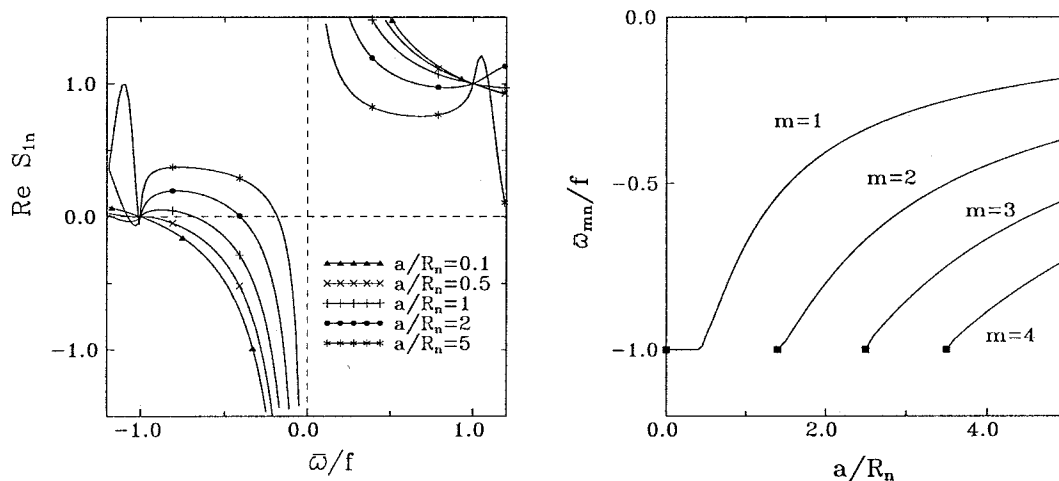


Figure 1: The real part of  $S_{1n}$  as a function of  $\bar{\omega}$  (left figure) and the Kelvin wave frequency  $\bar{\omega}_{mn}$  as a function of  $\frac{a}{R_n}$  for different values of  $m$  (right figure). The filled squares mark the critical radius  $a_{mn}^{crit}$ .

There is no trapped solution for  $m = 0$ . For  $m = \pm 1$  the critical radius is zero. As a special property of this mode which is forced by a homogeneous upstream flow a trapped solution exists also for islands with a small radius. However, the trapping is weak, since for  $R_0 \gg a$  the wave frequency is approximately

$$\bar{\omega}_{10} \approx -f + 2f \frac{R_0^2}{a^2} e^{-\left(\frac{R_0^2}{a^2} + 2\gamma\right)}. \quad (2.87)$$

So the arguments of the Bessel functions are small and decrease slowly even for large radii.

The left part of Fig. 1 shows the real part of  $S_{1n}$  as a function of  $\bar{\omega}$  for different values of  $\frac{a}{R_n}$ . All graphs run through the point  $\bar{\omega} = -f$ . If the

ratio  $\frac{a}{R_n}$  is large, a well distinct second zero exists corresponding to a trapped (Kelvin) wave. The right part of Fig. 1 shows the value of this Kelvin wave frequency as function of  $\frac{a}{R_n}$  for different values of the angular mode number  $m$ . The squares mark the critical radius  $a_{mn}^{crit}$ .

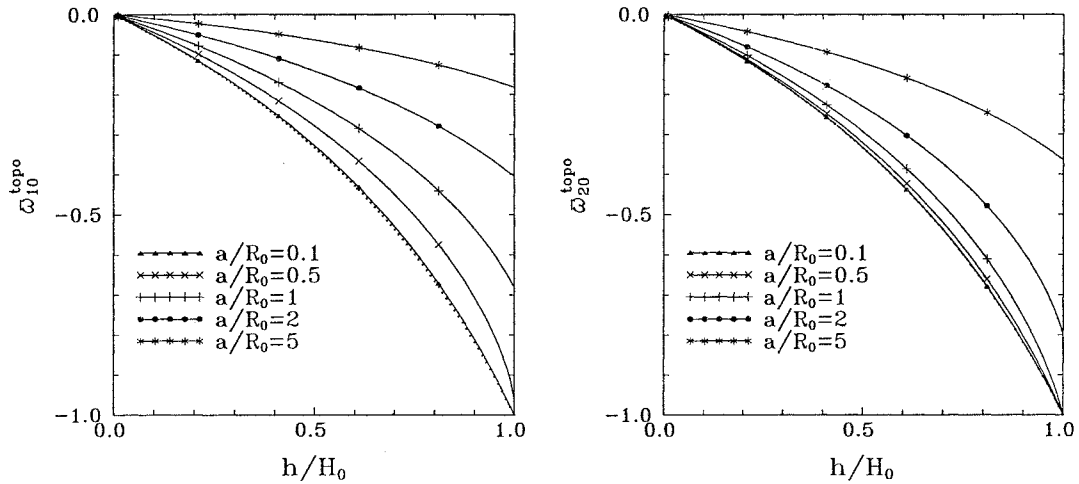


Figure 2: The topographic frequency  $\bar{\omega}_{mb}^{topo}$  as a function of  $\frac{h}{H_0}$  for different values of  $\frac{a}{R_0} \ll 1$ , left:  $m = 1$ , right:  $m = 2$ . The dotted line is the approximation according to eq. (2.92) for  $a \ll R_0$

Now we let the island “sink down” and get a seamount. The change in the spectrum can be understood from Fig. 1 and eq. (2.73). The curves for  $S_m(\omega)$  are shifted upwards. If there is a well distinct Kelvin wave trapped at an island, its frequency value is lowered with decreasing obstacle height  $h$ . If the obstacle radius is small, i.e., if there are near inertial waves generated at the island, the change in the frequency spectrum is more dramatic with decreasing  $h$ . The zero at the inertial frequency moves rapidly to lower values of  $\bar{\omega}$ , i.e. the waves become trapped.

Rewriting the denominator of  $\psi$  as

$$\bar{\omega}\sigma_{m0}(\omega)D_{m0} = W_{|m|}(\omega) \left( \bar{\omega} + mf \frac{h}{H_0} \frac{I_m(\beta a) K_m(\alpha_0 a)}{W_{|m|}(\omega)} \right), \quad (2.88)$$

$$W_{|m|}(\omega) = \alpha_0 a \left( \tilde{\beta}^{-1} I'_{|m|}(\beta a) K_m(\alpha_0 a) - I_{|m|}(\beta a) K'_m(\alpha_0 a) \right), \quad (2.89)$$

the structure is more transparent.  $W_{|m|}(\omega)$  is positive definite. There is one solution  $\bar{\omega}_{mb}^{topo}$  corresponding to a trapped wave which will be called subsequently

"topographic frequency". The subscript  $_b$  stands for "barotropic approximation" in the sense of "depth independent" rather than for "barotropic mode". Fig. 2 shows the topographic frequency calculated numerically from eq. (2.88) as function of the relative topographic height  $\frac{h}{H_0}$ . The modulus of the frequency decreases with  $h$ , the frequency of a Kelvin wave trapped at an island with radius  $a$  appears as an upper bound for the topographic frequency of waves trapped at a cylindrical obstacle.

For the two limiting cases  $\tilde{\beta}a \ll R_0$  and  $a \gg R_0$  analytical approximations for  $\bar{\omega}_{mb}^{topo}$  can be found. If the obstacle radius is small compared to the Rossby radius,  $\tilde{\beta}a \ll R_0$ , the topographic frequency reads for  $m = \pm 1$

$$\bar{\omega}_{mb}^{topo} \approx -mf \frac{h}{2H_0 - h} \left( 1 + \frac{H}{2H_0 - h} \frac{s^2}{4} \left( 4\gamma - 1 + 2 \ln \left( \frac{s^2}{4} \right) \right) \right), \quad (2.90)$$

$$s^2 = \frac{(f^2 - \bar{\omega}_{mb}^{topo2}) a^2}{f^2 R_0^2}. \quad (2.91)$$

$s^2$  tends to zero if the island radius is small compared to the Rossby radius and the rigid lid approximation is valid. In this case the right hand side of eq. (2.90) is independent of  $\bar{\omega}_{mb}^{topo}$  and the topographic frequency depends on the inertial frequency  $f$  and the relative height  $\frac{h}{H_0}$  of the obstacle only,

$$\bar{\omega}_{mb}^{topo} \approx -mf \frac{h}{2H_0 - h} \quad \text{for } a \ll R_0. \quad (2.92)$$

The above rigid lid approximation provides an upper limit for the modulus of the topographic frequency.

If the relative height of the obstacle is small, the topographic frequency is much smaller than  $f$ . This allows an iterative solution of eq. (2.88). The first order approximation is valid for  $\frac{h}{H_0} \ll 1$  and reads

$$\bar{\omega}_{mb}^{topo} \approx -mf \frac{h}{H_0} \frac{I_m \left( \tilde{\beta} \frac{a}{R_0} \right) K_m \left( \frac{a}{R_0} \right)}{\frac{a}{R_0} \left( \tilde{\beta}^{-1} I'_{|m|} \left( \tilde{\beta} \frac{a}{R_0} \right) K_m \left( \frac{a}{R_0} \right) - I_{|m|} \left( \tilde{\beta} \frac{a}{R_0} \right) K'_m \left( \frac{a}{R_0} \right) \right)}, \quad (2.93)$$

$$\approx -mf \frac{h}{H_0} I_m \left( \tilde{\beta} \frac{a}{R_0} \right) K_m \left( \frac{a}{R_0} \right). \quad (2.94)$$

Fig. 2 gives a guide, where this approximation is applicable. The rigid lid approximation eq. (2.92) follows as a special case of eq. (2.93) for  $\tilde{\beta}a \ll R_0$ .

For  $a \gg R_0$  the topographic frequency is proportionally to the frequency of a Kelvin wave trapped at the obstacle edge

$$\bar{\omega}_{mb}^{topo} \approx \frac{h}{H_0} \frac{\tilde{\beta}}{1 + \tilde{\beta}} \bar{\omega}_{m0} \quad \text{for } a \gg R_0. \quad (2.95)$$

The topographic frequency  $\bar{\omega}_{mb}^{topo}$  depends on the relative obstacle height  $\frac{h}{H_0}$  only but is independent of the total depth  $H_0$  and the obstacle height  $h$  itself. This stems from the fact that the topographic waves propagate as vorticity waves generated by compressing or stretching of vorticity lines at the gradients of the bottom topography.

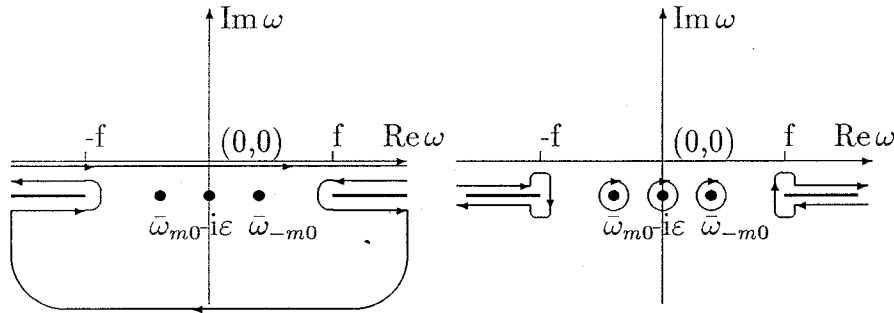


Figure 3: The relevant singularities and the integration path in the complex  $\omega$  plane.

Let us now discuss the time evolution of the flow pattern. This requires the inverse Fourier transformation of eq.s (2.68) and (2.69) which can be performed using Cauchy's theorem. To get a closed integration path in the complex  $\omega$ -plane we complete the integral along the real axis by a semicircle in the upper or lower half-plane. It depends on the behavior of  $\psi(\omega)$  for  $\omega \rightarrow \pm i\infty$  whether the integration path can be closed in the upper or the lower half-plane. Setting  $\omega = iq$  we find

$$e^{-i\omega t} \psi_{m0}^a(r a \omega) \sim \frac{e^{\left(t - \frac{r-a}{f R_0}\right) q}}{q}, \quad (2.96)$$

$$e^{-i\omega t} \psi_{m0}^i(r a \omega) \sim \frac{e^{\left(t - \frac{a-r}{f R_0} \tilde{\beta}\right) q}}{q}. \quad (2.97)$$

This expression tends to zero if

$$\left. \begin{array}{l} t > \frac{r-a}{fR_0} \quad \text{for} \quad q \rightarrow -\infty \\ t < \frac{r-a}{fR_0} \quad \text{for} \quad q \rightarrow \infty \end{array} \right\} \quad r > a$$

$$\left. \begin{array}{l} t > \frac{a-r}{fR_0} \tilde{\beta} \quad \text{for} \quad q \rightarrow -\infty \\ t < \frac{a-r}{fR_0} \tilde{\beta} \quad \text{for} \quad q \rightarrow \infty \end{array} \right\} \quad r < a.$$

Fig. 3 shows the relevant singularities. Closing the integration path in the upper half plane it can be contracted to a point without enclosing a singularity. Consequently, the Fourier transform of  $\psi_{m0}^a$  vanishes for  $t < \frac{r-a}{fR_0}$ . For  $t > \frac{r-a}{fR_0}$  it can be expressed by a Cauchy integral closed in the lower half plane. A similar behavior can be found for  $\psi_{m0}^i$ . Besides the poles with  $|\bar{\omega}| < f$  corresponding to the trapped waves we have to consider the branch points of  $\sqrt{f^2 - \bar{\omega}^2}$  at  $\omega = \pm f - i\nu$ . Rewriting

$$\alpha_0 = \frac{1}{R_0} \sqrt{f - \omega - i\nu} \sqrt{f + \omega + i\nu} \quad (2.98)$$

it turns out that we need two cuts to make  $\alpha_0$  unique. Choosing the cuts parallel to the real axis according to Fig. 3 the imaginary part of  $\alpha_0$  is always positive and the cut of the Hankel function needs no special consideration. However, we are not allowed to cross the line  $Im(\omega) = -i\nu$  at  $|Re(\omega)| > f$ . The integral over the cuts which have been added to close the contour does not vanish and we have to subtract this contribution from the total integral over the closed contour. The second part of Fig. 3 shows the remaining path integrals after contracting the whole contour to separate contour lines encircling the singularities.

Subsequently, we will consider only the trapped waves, i.e., we take into account only the integrals encircling the singularities at  $\bar{\omega} = 0$  and  $\bar{\omega} = \bar{\omega}_{mb}^{topo}$ . However, this approximation has to be considered with some caution if the frequency of the trapped waves is near the inertial frequency, i.e. if  $h \approx H_0$  and  $a \ll R_0$ . Although the approximation (2.93) is suitable to calculate the spectrum, the calculation of the residuum is more delicious and requires a

detailed discussions of all parts of the spectrum. Especially for islands with a small radius,  $a \ll R_0$ , the integral along the cuts compensates partially the contribution of the trapped waves. This problem will be discussed elsewhere.

Here, we restrict ourselves to situations where the frequency of the trapped waves is well distinct from the inertial frequency, i.e.  $\tilde{\beta}a \ll R_0$  or  $a \gg R_0$ . For reasons of consistency we neglect in all expressions  $\bar{\omega}$  in comparison with  $f$ , i.e., in the numerator of  $\psi$  and in the arguments of the Bessel functions and calculate the topographic frequency from the approximation eq. (2.93). This is necessary to fulfill the boundary condition (2.67) for the radial transport. The denominator of  $\psi$  reads approximately

$$\bar{\omega}\sigma_{m0}(\omega)D_{m0} \approx -\frac{h}{H_0}f \frac{I_m\left(\tilde{\beta}\frac{a}{R_0}\right)K_m\left(\frac{a}{R_0}\right)}{\bar{\omega}_{1b}^{topo}} \left(\bar{\omega} - m\bar{\omega}_{1b}^{topo}\right). \quad (2.99)$$

For the Fourier transformation the upstream flow has to be specified. We consider the example of a flow switched on at  $t = 0$  and staying constant thereafter. The Fourier transformed reads

$$u_0(\omega) = U_0 \frac{i}{\omega + i\varepsilon}. \quad (2.100)$$

(Other examples, i.e. an oscillating upstream flow, but within a perturbational solution scheme valid for small topography, has been considered by FENNEL and SCHMIDT (1991).)  $u_0$  is undamped, and the frequency  $\omega$  has to be distinguished carefully from  $\bar{\omega}$ .

The pressure perturbation is a product of an amplitude function  $\Gamma(r)$  describing the radial shape of  $\psi$  and a factor  $Q(\varphi t)$  standing for a angular wavelike time evolution of  $\psi$ .

$$\psi^a(r\varphi t) = \theta\left(t - \frac{r-a}{R_0f}\right) fU_0a\Gamma^a(r)Q(\varphi t), \quad (2.101)$$

$$\psi^i(r\varphi t) = \theta\left(t - \tilde{\beta}\frac{a-r}{R_0f}\right) fU_0a\Gamma^i(r)Q(\varphi t). \quad (2.102)$$

The radial function  $\Gamma$  reads

$$\Gamma^a(r) = \frac{K_1\left(\frac{r}{R_0}\right)}{K_1\left(\frac{a}{R_0}\right)}, \quad (2.103)$$

$$\Gamma^i(r) = \frac{I_1\left(\tilde{\beta}\frac{r}{R_0}\right)}{I_1\left(\tilde{\beta}\frac{a}{R_0}\right)}. \quad (2.104)$$

Outside of the obstacle  $\Gamma(r)$  decreases exponentially for distances larger than the barotropic Rossby radius. Over the obstacle the pressure perturbation is also trapped at the edge but the characteristic distance

$$\frac{R_0}{\tilde{\beta}} = \frac{1}{f} \sqrt{gH_0} \sqrt{\frac{H_0 - h}{H_0}} = \frac{\sqrt{g(H_0 - h)}}{f} \quad (2.105)$$

is a reduced Rossby radius corresponding to the reduced depth over the obstacle,  $H_0 - h$ . If the radius of the obstacle  $a$  is much smaller than this Rossby radius the pressure perturbation decreases linearly from the edge to the obstacle center.

Initially, after the upstream flow has been switched on, the information on the obstacle perturbing the upstream flow spreads by inertial waves over the whole basin. Outside the obstacle their phase speed is  $R_0 f$ , over the obstacle the phase speed is reduced by a factor  $\tilde{\beta}^{-1}$ . The inertial waves are not considered explicitly and the step functions in the expression for  $\psi$  are the remainder of this initial process.

In addition to this radially spreading wave front there is a topographic wave orbiting clockwise round the obstacle. This wave process is represented by the factor

$$Q(\varphi t) = \frac{\omega_{1b}^{topo}}{\omega_{1b}^{topo/2} + \nu^2} \left( \omega_{1b}^{topo} q_s(\varphi, t) + \nu q_c(\varphi, t) \right) \quad (2.106)$$

with the abbreviations

$$q_s(\varphi, t) = \sin \varphi - e^{-\nu t} \sin(\varphi - \omega_{1b}^{topo} t), \quad (2.107)$$

$$q_c(\varphi, t) = \cos \varphi - e^{-\nu t} \cos(\varphi - \omega_{1b}^{topo} t). \quad (2.108)$$

The radial and angular components of the velocity field (transport) are related to the pressure perturbation via

$$u_m^r = u_{0m}^r + \frac{i\bar{\omega}}{f^2 - \bar{\omega}^2} \left( \frac{\partial \psi_m}{\partial r} - \frac{mf}{\bar{\omega}r} \psi_m \right) \quad (2.109)$$

$$u_m^\varphi = u_{0m}^\varphi + \frac{\bar{\omega}}{f^2 - \bar{\omega}^2} \left( \frac{f}{\bar{\omega}} \frac{\partial \psi_m}{\partial r} - \frac{m}{r} \psi_m \right) \quad (2.110)$$

For a homogeneous upstream flow,

$$u_{0m}^r = u_0 \pi \delta_{|m|1}, \quad (2.111)$$

$$u_{0m}^\varphi = i u_0 \pi \delta_{|m|1} \text{sig}(m), \quad (2.112)$$

the time evolution of the flow near the obstacle is governed by topographic waves with the frequency  $\omega_{1b}^{topo}$ ,

$$\begin{aligned}
u^r(r\varphi t) \approx & U_0 \cos \varphi \left( \theta(t) - \theta \left( t - \frac{r-a}{R_0 f} \right) \frac{a}{r} \Gamma(r) \right) \\
& + U_0 \theta \left( t - \frac{r-a}{R_0 f} \right) \left( \frac{a}{r} \Gamma(r) - \frac{a \omega_{1b}^{topo}}{f} \frac{\partial \Gamma}{\partial r} \right) \left( e^{-\nu t} \cos \left( \varphi - \omega_{1b}^{topo} t \right) \right. \\
& + \frac{\nu}{\omega_{1b}^{topo 2} + \nu^2} \left( \nu \cos \varphi + \omega_{1b}^{topo} \sin \varphi \right. \\
& \left. \left. - e^{-\nu t} \left( \nu \cos \left( \varphi - \omega_{1b}^{topo} t \right) + \omega_{1b}^{topo} \sin \left( \varphi - \omega_{1b}^{topo} t \right) \right) \right) \right), \quad (2.113)
\end{aligned}$$

$$\begin{aligned}
u^\varphi(r\varphi t) \approx & -U_0 \sin \varphi \left( \theta(t) - \theta \left( t - \frac{r-a}{R_0 f} \right) a \frac{\partial \Gamma}{\partial r} \right) \\
& - U_0 \theta \left( t - \frac{r-a}{R_0 f} \right) \left( a \frac{\partial \Gamma}{\partial r} - \frac{a \omega_{1b}^{topo}}{r f} \Gamma(r) \right) \left( e^{-\nu t} \sin \left( \varphi - \omega_{1b}^{topo} t \right) \right. \\
& + \frac{\nu}{\omega_{1b}^{topo 2} + \nu^2} \left( \nu \sin \varphi - \omega_{1b}^{topo} \cos \varphi \right. \\
& \left. \left. - e^{-\nu t} \left( \nu \sin \left( \varphi - \omega_{1b}^{topo} t \right) - \omega_{1b}^{topo} \cos \left( \varphi - \omega_{1b}^{topo} t \right) \right) \right) \right). \quad (2.114)
\end{aligned}$$

The rigid lid result as discussed by JOHNSON (1984) is reclaimed in the limit  $\tilde{\beta} \frac{a}{R_0} < 1$  and for small topography,  $\frac{h}{H_0} \ll 1$ . Since this case occurs frequently in oceanography, it should be discussed in more detail. For  $\tilde{\beta} \frac{a}{R_0} < 1$  the velocity components  $u^r$  and  $u^\varphi$  are

$$\begin{aligned}
u^{ar}(r\varphi t) \approx & U_0 \theta(t) \left( \left( 1 - \frac{a^2}{r^2} \right) \cos \varphi + \frac{a^2}{r^2} \left( 1 + \frac{\omega_{1b}^{topo}}{f} \right) \frac{1}{\omega_{1b}^{topo 2} + \nu^2} \right. \\
& \left. \left( \nu^2 \cos \varphi + \nu \omega_{1b}^{topo} \sin \varphi \right. \right. \\
& \left. \left. + e^{-\nu t} \omega_{1b}^{topo} \left( \omega_{1b}^{topo} \cos \left( \varphi - \omega_{1b}^{topo} t \right) - \nu \sin \left( \varphi - \omega_{1b}^{topo} t \right) \right) \right) \right), \quad (2.115)
\end{aligned}$$

$$\begin{aligned}
u^{i\varphi}(r\varphi t) \approx & U_0 \theta(t) \left( \left( 1 - \frac{\omega_{1b}^{topo}}{f} \right) \frac{1}{\omega_{1b}^{topo 2} + \nu^2} \right. \\
& \left. \left( \nu^2 \cos \varphi + \nu \omega_{1b}^{topo} \sin \varphi \right. \right. \\
& \left. \left. + e^{-\nu t} \omega_{1b}^{topo} \left( \omega_{1b}^{topo} \cos \left( \varphi - \omega_{1b}^{topo} t \right) - \nu \sin \left( \varphi - \omega_{1b}^{topo} t \right) \right) \right) \right), \quad (2.116)
\end{aligned}$$

$$\begin{aligned}
u^{a\varphi}(r\varphi t) \approx & -U_0\theta(t) \left( \left( 1 + \frac{a^2}{r^2} \right) \sin \varphi - \frac{a^2}{r^2} \left( 1 + \frac{\omega_{1b}^{topo}}{f} \right) \frac{1}{\omega_{1b}^{topo 2} + \nu^2} \right. \\
& \left( \nu^2 \sin \varphi - \omega_{1b}^{topo} \nu \cos \varphi \right. \\
& \left. \left. + \omega_{1b}^{topo} e^{-\nu t} \left( \omega_{1b}^{topo} \sin \left( \varphi - \omega_{1b}^{topo} t \right) + \nu \cos \left( \varphi - \omega_{1b}^{topo} t \right) \right) \right) \right),
\end{aligned} \tag{2.117}$$

$$\begin{aligned}
u^{i\varphi}(r\varphi t) \approx & +U_0\theta(t) \left( \left( 1 - \frac{\omega_{1b}^{topo}}{f} \right) \frac{1}{\omega_{1b}^{topo 2} + \nu^2} \right. \\
& \left( -\nu^2 \sin \varphi + \nu \omega_{1b}^{topo} \cos \varphi \right. \\
& \left. \left. - \omega_{1b}^{topo} e^{-\nu t} \left( \omega_{1b}^{topo} \sin \left( \varphi - \omega_{1b}^{topo} t \right) + \nu \cos \left( \varphi - \omega_{1b}^{topo} t \right) \right) \right) \right).
\end{aligned} \tag{2.118}$$

Fig. 4 shows a sketch of six snapshots of the flow over the obstacle during one cycle of the topographic wave in the inviscid case,  $\nu = 0$ . The perturbation in the sea level has a maximum at the obstacle edge and travels clockwise round the obstacle. The corresponding flow field follows the isobars. There are ageostrophic flow components which, however, do not alter the flow direction but decrease the magnitude by a factor  $\approx 1 - \frac{h}{2H_0 - h}$ .

Outside of the obstacle the flow is a linear superposition of the upstream flow and a dipole like perturbation. Over the topography the flow is homogeneously. The modulus is independent of time, whereas the flow direction rotates with the frequency  $-\omega_{1b}^{topo}$ . The radial transport is continuously at the edge of the obstacle but the angular transport exhibits a jump corresponding to a vorticity sheet at  $r = a$ . Partially closed streamlines occur independent of the obstacle height and the upstream velocity.

If viscosity is present, i.e.  $\nu > 0$ , the time dependent flow part tends to zero after some oscillations and the vorticity production at the obstacle edge is balanced by dissipation. The flow is controlled by friction and approximately geostrophically balanced. The zero line of the stationary dipole like pressure field is twisted by an angle

$$\varphi_\infty = \arctan \left( -\frac{\nu}{\omega_{1b}^{topo}} \right) \tag{2.119}$$

compared to the direction of the upstream flow.

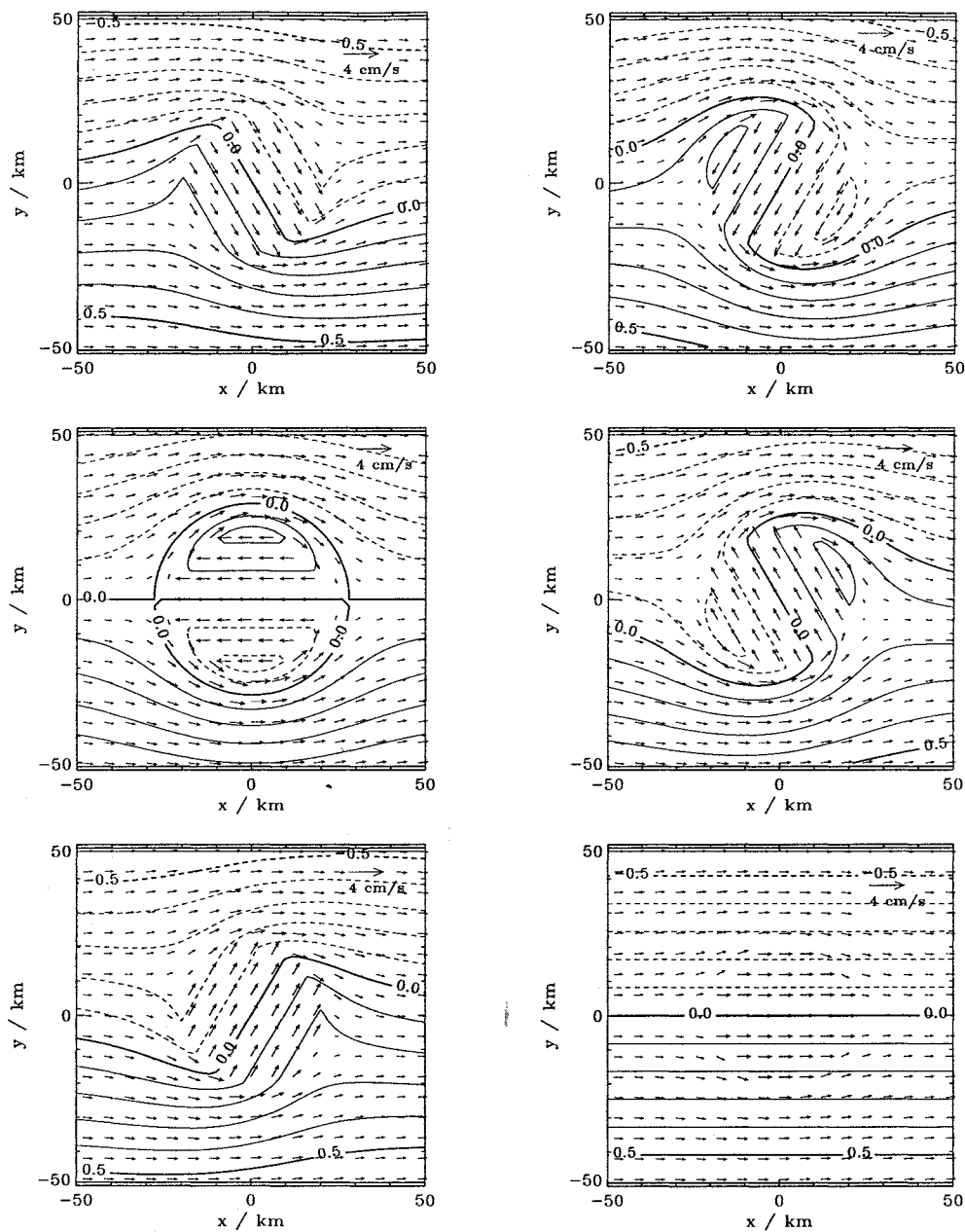


Figure 4: First cycle of the evolution of the topographic waves in time steps of  $\omega_{1b}^{topo} t = \frac{\pi}{3}$ . Isolines of the sealevel and the flow velocity are shown. The parameters are  $\frac{h}{H_0} = 0.667$ , obstacle radius  $a = 20$  km,  $R_0 \approx 140$  km, friction parameter  $\nu = 0$ . The topographic frequency is  $\omega_{1b}^{topo} = -0.48f$ . The geostrophic upstream flow coming from the left hand side is set to  $1 \text{ cm s}^{-1}$ .

If the friction parameter is of the same order of magnitude as the topographic frequency, the stationary flow over the obstacle is of the same order

of magnitude as the upstream flow too. This may be the case especially for small seamounts where the topographic frequency is small. If the friction parameter  $\nu$  is much smaller than the topographic frequency  $\omega_{1b}^{topo}$  the stationary flow remaining over the obstacle is much smaller than the upstream flow and the angle  $\varphi_\infty$  tends to zero. Almost all water particles originating upstream pass the topography at a path beside the obstacle. Examples for frictionally controlled stationary states are shown in Fig. 5. The stationary pressure perturbation following from eq. (2.102) is equivalent to the result of HICKIE (1972).

These stationary states are sometimes related to Taylor columns and called "frictionally balanced Taylor columns". However, this may be misleading because no closed streamlines occur and the underlying physics is completely different.

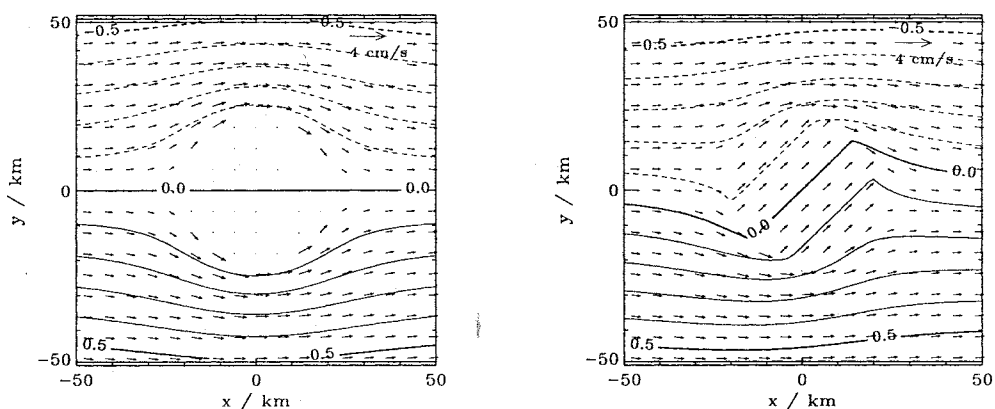


Figure 5: Stationary states controlled by friction for  $\nu = \frac{f}{50}$  (left picture) and  $\nu = |\omega_{1b}^{topo}|$  (right picture). The parameters are the same as in Fig. 4.

The consideration of the case  $R_0 \ll a$  is of rather theoretical value, since the assumption of a homogeneous upstream flow with a horizontal extent larger than the barotropic Rossby radius is more or less artificial. However, this limit shows the influence of the trapping of the pressure perturbation at the obstacle edge which plays an important role also for the baroclinic modes. The result may be considered as the lowest order term of a decomposition into angular modes.

Considering the lowest order of  $\frac{R_0}{a}$  the radial and vertical velocity simplifies for the inviscid case

$$u^{ar}(r\varphi t) \approx U_0\theta(t) \cos \varphi - U_0\theta \left( t - \frac{r-a}{R_0 f} \right) \sqrt{\frac{a}{r}} e^{-\frac{r-a}{R_0}} \left( \frac{a}{r} \cos \varphi - \left( \frac{a}{r} - \frac{h}{H_0} \frac{\tilde{\beta}}{1+\tilde{\beta}} \right) \cos \left( \varphi - \omega_{1b}^{topo} t \right) \right), \quad (2.120)$$

$$u^{ir}(r\varphi t) \approx U_0\theta(t) \cos \varphi - U_0\theta \left( t - \tilde{\beta} \frac{a-r}{R_0 f} \right) \left( \frac{a I_1(\beta r)}{r I_1(\beta a)} \cos \varphi - \left( \frac{a I_1(\beta r)}{r I_1(\beta a)} + \frac{h}{H_0} \frac{\tilde{\beta}^2}{1+\tilde{\beta}} \frac{I_2(\beta r)}{I_1(\beta a)} \right) \cos \left( \varphi - \omega_{1b}^{topo} t \right) \right). \quad (2.121)$$

$$u^{a\varphi}(r\varphi t) \approx -U_0\theta(t) \sin \varphi - U_0\theta \left( t - \frac{r-a}{R_0 f} \right) \sqrt{\frac{a}{r}} e^{-\frac{r-a}{R_0}} \frac{a}{R_0} \left( \sin \varphi - \sin \left( \varphi - \omega_{1b}^{topo} t \right) \right), \quad (2.122)$$

$$u^{i\varphi}(r\varphi t) \approx -U_0\theta(t) \sin \varphi + U_0\theta \left( t - \tilde{\beta} \frac{a-r}{R_0 f} \right) \tilde{\beta} \frac{a}{R_0} \frac{I_2(\beta r)}{I_1(\beta a)} \left( \sin \varphi - \sin \left( \varphi - \omega_{1b}^{topo} t \right) \right). \quad (2.123)$$

The flow perturbation is trapped within a distance of  $R_0$  at the edge of the obstacle and rotates clockwise with a frequency  $\omega_{1b}^{topo}$ . An approximation for the frequency is given as a function of  $\frac{h}{H_0}$  by eq. (2.95). Fig. 6 shows two examples for the evolution of the flow at the obstacle in the frictionless limit.

Remarkably, the radial flow generated at the obstacle is of higher order in  $\frac{R_0}{a}$  than the angular flow. Consequently, the flow perturbation consists of well pronounced angular jets corresponding to a vorticity sheet at  $r = a$ . At the obstacle edge the radial flow is purely oscillating. The order of magnitude is  $U_0$  and the average over one cycle of the radial transport vanishes. The angular flow is of the order  $\frac{a}{R_0}$  and is strongly enhanced. Since the radial derivative of  $u^r$  is larger by a factor  $\frac{a}{R_0}$  than the angular derivative of  $u^\varphi$  by, both velocity components contribute with the same order of magnitude to the horizontal flow divergence.

The angular jets at the edge of the topography are fed by the water masses which do not pass over the topography. Beside the obstacle the amplitude of the jet is independent of the obstacle height. Over the obstacle the trapping radius becomes smaller with increasing height so the flow perturbation for high obstacles is confined to a thin area at the edge. In the island limit the

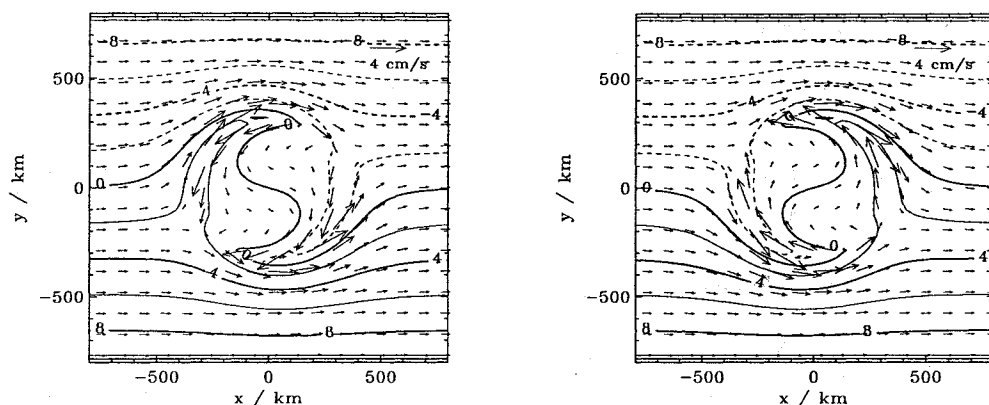


Figure 6: Surface elevation and flow field for  $|\omega_{1b}^{topo}|t = \frac{2\pi}{3}$  and  $|\omega_{1b}^{topo}|t = \frac{4\pi}{3}$ . The parameters are  $\frac{h}{H_0} = 0.667$ , obstacle radius  $a = 320$  km,  $R_0 \approx 140$  km, friction parameter  $\nu = 0$ . The topographic frequency is  $\omega_{1b}^{topo} = 0.17f$ . The geostrophic upstream flow coming from the left hand side is set to  $1 \text{ cm s}^{-1}$ .

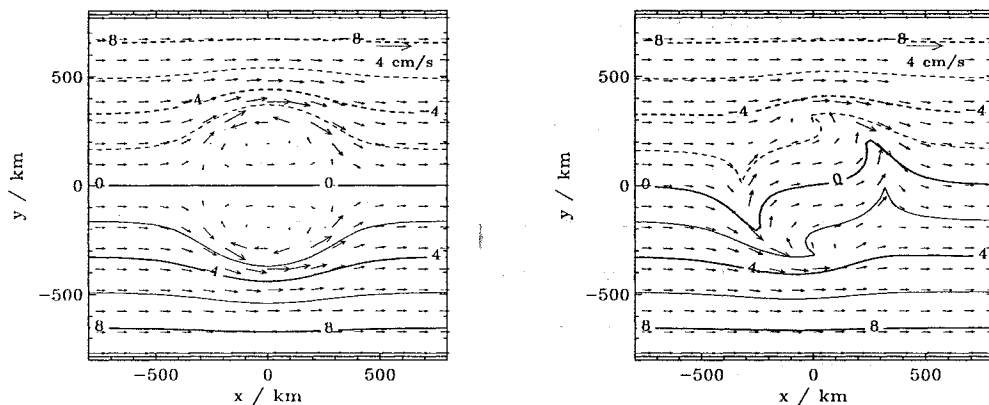


Figure 7: Stationary states controlled by friction for  $\nu = \frac{f}{50}$  (left picture) and  $\nu = |\omega_{1b}^{topo}|$  (right picture). The parameters are the same as in Fig. 6.

vertically integrated radial velocity vanishes at the edge of the obstacle as well as over the obstacle itself. The angular velocity over the obstacle at  $r = a$ ,  $u^{i\varphi}(a)$ , is not well defined and becomes infinitely large for  $h \rightarrow H_0$ . However, the vertically integrated flow vanishes.

In the viscous stationary state the radial velocity component vanishes at

the edge of the obstacle for small  $\nu$ . Then, the flow beside and over the obstacle is separated by the vorticity sheet. Nevertheless, the flow over the obstacle does not vanish as in the viscous rigid lid case. On the contrary, the pressure perturbation is trapped within a distance  $\tilde{\beta}R_0$  at the obstacle edge and the flow over the center of the obstacle is approximately the original upstream flow. The streamlines are closed by the inner jets at the edge of the topography. These jets at the inner edge keep the inner flow running even in the viscous case. The jet itself is in geostrophic balance with the radial pressure gradient. This stationary state is shown in the left part of Fig. 7. The right part of this Fig. 7 corresponds to the case  $\nu = |\omega_{1b}^{topo}|$ .

The present calculation does not distinguish vertical and lateral friction. It can be expected, that the vorticity sheet is smoothed if lateral friction is included. However, it remains an open question, whether the motion over the obstacle is only diminished by lateral momentum exchange or if the flow over the topography is completely spun down.

### 2.5.2 Baroclinic approximations

In this section the considerations for the barotropic approximation are generalized to include the influence of stratification. The changes due to stratification concern both the spectrum of the topographic waves as well as the flow pattern. Two approximation schemes for solving the baroclinic equation are discussed. One is based on the assumption that the pressure perturbation at the sidewall of the obstacle is approximately constant, i.e.  $\psi_m(z < -H_0 + h) \approx \psi_m(-H_0 + h)$ . This approximation may be justified if the stratification is weak or the topography is of small height. The other approximation scheme is based on a decomposition of  $\psi_m(z)$  into vertical eigenfunctions. Since all vertical modes are coupled via the bottom boundary condition the integral equation for the pressure is transformed into a linear system of equations of rank infinity which has to be reduced to a finite amount of equations. This approximation is good, if only a small amount of vertical modes is necessary to approximate the complete solution. For high seamounts it is an alternative for the first approximation scheme which fails in this case. In both schemes the first term in eq. (2.61) is calculated by iteration starting with the onset

of a pressure perturbation over the topography proportional to the barotropic solution.

We begin the discussion with the iterative solution scheme. Details are given in Appendix C.1. As in the barotropic case, the spectrum follows from the zeros of the denominator of the pressure perturbation. This approximation allows for one topographic mode. Assuming a constant Brunt Väisälä frequency, for an obstacle with a diameter much smaller than the barotropic Rossby radius,  $R_0 \gg a$ , but larger than the baroclinic Rossby radius,  $R_1 \ll a$ , the pressure perturbation at  $r = a$  simplifies considerably, all mode sums can be performed analytically (Appendix C.1). The topographic frequency reads approximately

$$\omega_m^{topo} \approx -f \frac{h \left( \text{sgn}(m) + \frac{m2R_1}{a} \left( 1 - \ln \left( \frac{2\pi h}{H_0} \right) \right) \right)}{2H_0 - h - \frac{h|m|2R_1}{a} \left( 1 - \ln \left( \frac{2\pi h}{H_0} \right) \right)}. \quad (2.124)$$

This approximation is valid for  $\frac{h}{H_0} < \frac{1}{4}$ . A more general result is given in Appendix C.1.

For weak stratification the barotropic result for  $R_0 \gg a$ , eq. (2.92) is retained. Stratification increases the frequency of the trapped wave because a pycnocline acts in a similar manner as the sea surface and yields an effective decrease of the total depth.

To avoid confusion we have to distinguish the wave modes corresponding to barotropic and baroclinic vertical eigenfunctions with respect to the flat bottom ocean from the topographic wave modes. Except Kelvin waves trapped at an island each topographic mode is build up by contributions coming from all flat bottom vertical eigenfunctions, i.e., from the barotropic and all baroclinic modes.

At an island with steep sidewalls besides the barotropic Kelvin wave a large variety of baroclinic Kelvin waves may be excited. The vertical structure of these waves is governed by the baroclinic vertical eigenfunctions for a flat bottom ocean. It is natural to ask which topographic wave modes correspond to the baroclinic Kelvin waves if the island is replaced by a finite height seamount. Picking up a special mode in the island case and replacing the island by a seamount, the change of the wave frequency can be traced. Thus, the topographic modes may be labeled by the mode numbers of the vertical

modes in the island case. The iterative approximation scheme as given above allows for only one topographic mode in the first iteration step. Other modes can be found by further iteration.

Now we consider the alternative solution method by decomposition into vertical eigenfunctions. The integral equation (2.61) is transformed into a linear system of equations of rank infinity, eq. (C.34). The details are given in Appendix C.2. The equation for  $\psi$  has been rearranged in such a way, eq. (C.10), that all contributions are well convergent sums. Thus, the linear system of rank infinity can be replaced approximately by a system of finite rank. If the number of modes involved is  $n$ , there are  $n$  zeros of the determinant of the homogeneous system, eq. (C.41), which define the spectrum of the topographic waves. In the island case the coefficient matrix is diagonal and the frequency spectrum of Kelvin waves trapped at the island is retained. Since the vertical modes separate, the truncation of the mode sums does not influence the remaining wave spectrum.

For an obstacle each topographic mode consists of a superposition of all flat bottom vertical eigenfunctions. The larger the mode coupling, i.e. the smaller the height of the seamount is, the more vertical modes have to be included. This stems from the coupling matrix  $M_{nl}$ . Comparing diagonal and off-diagonal matrix elements, for high seamounts the diagonal elements dominate, whereas for seamounts of small height both are of the same order of magnitude. This may be of importance for the interpretation of numerical results from finite difference models. Due to the finite horizontal and vertical resolution those schemes filter out higher modes. We will come back to this point in section 3.

Eq. (C.41) has been solved including the barotropic and 19 baroclinic eigenfunctions. Thus, for each value of  $\frac{h}{H_0}$  20 topographic modes can be found. In Fig. 8 the frequency of the five lowest topographic modes is shown as a function of the relative height  $\frac{h}{H_0}$ . It has been tested that the inclusion of additional vertical modes does not alter the frequency of these topographic wave modes. In the island limit,  $\frac{h}{H_0} = 1$ , the topographic waves are going over into the barotropic and the first four baroclinic Kelvin waves. The dotted line is the barotropic approximation which is obtained, if only the barotropic vertical

mode is included. It is equivalent to the barotropic result as discussed in the previous section. The difference between the barotropic approximation and the baroclinic result shows that stratification may increase the topographic frequency considerably. Since mode coupling is growing with decreasing obstacle height, the frequency enhancement is most obvious for small obstacles.

The dashed line shows the iterative approximation based on eq. (C.15). It may be used as a guide for the order of magnitude of baroclinic effects but fails for seamounts with a height  $\frac{h}{H_0} > \frac{1}{2}$ . The value of the crossing point with the barotropic approximation at  $\frac{h}{H_0} = \frac{1}{2}$  stems from the special choice of the stratification.

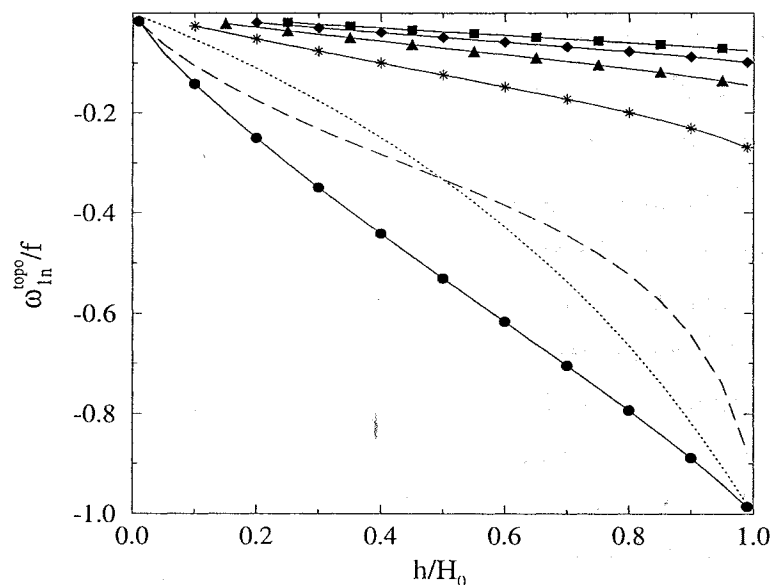


Figure 8: The spectrum of baroclinic topographic waves at a cylindrical seamount. Parameters: obstacle radius  $a = 6$  km,  $R_0 \approx 140$  km,  $R_1 \approx 2$  km. Dotted line ( $\cdot \cdot \cdot$ ): barotropic approximation, dashed line ( $- - -$ ): iterative solution according to eq. (C.15), ( $\bullet - \bullet$ ): most prominent topographic mode corresponding to a barotropic Kelvin wave in the island limit, other symbols: topographic modes corresponding to baroclinic Kelvin waves

The three-dimensional baroclinic pressure perturbation and the corresponding flow field can be calculated also from the aforementioned approximation schemes. Here, only the vertical structure of the pressure perturbation as well

as the vertical displacement of isopycnals is discussed basing on the iterative approximation scheme.

We start from eq.s (C.2) and (C.3). Considering the case that the topographic frequency is much smaller than the inertial frequency the approximation  $\alpha_n \approx R_n^{-1}$  is justified, whereby,  $R_n$  denotes the internal Rossby radius corresponding to the  $n$ 'th vertical (flat bottom) eigenfunction. As in the barotropic case a two-step solution is possible. In the first step an approximation for  $\psi(a, -H_0 + h)$ , eq. (C.14), can be found by iteration. This result is reinserted as an approximation for  $\psi(az)$  at the right hand side of eq.s (C.2 and (C.3). The details are given in Appendix C.1.

Since the iterative solution allows for only one topographic mode, the inverse Fourier transformation can be performed in the same manner as in the barotropic case. For simplicity we assume  $R_0 \gg R_1$ , which will be justified for the most applications. The pressure perturbation has the general form

$$\psi(r\varphi zt) \approx U_0 f a \Gamma_{bk}(rz) Q(\varphi t). \quad (2.125)$$

The function  $Q(\varphi t)$  differs from the barotropic approximation eq. (2.106) only by the value of the topographic frequency. The baroclinic amplitude function  $\Gamma_{bk}$  has a complicated structure. Here we discuss only the simple approximation

$$\Gamma_{bk}^{a/i}(rz) \approx \frac{\sum_n \int_{-H_0}^{-H_0+h} dz' F_n(z') F_n(z) \theta\left(t - \frac{r-a}{R_n f}\right) g_{mn}^{\geq}(ra)}{\sum_n \int_{-H_0}^{-H_0+h} dz' F_n(z') F_n(-H_0 + h) g_{mn}(aa)}, \quad (2.126)$$

which is valid for small topography,  $\beta \approx \alpha_0$ , and follows from eq. (C.32). In comparison with the barotropic approximation the barotropic contribution is supplemented by similar baroclinic contributions localized at the obstacle edge.

Fig. 9 shows the amplitude function  $\Gamma_{bk}(rz)$  for different values of the baroclinic Rossby radius. If the stratification is weak, (left picture), the pressure perturbation is mainly depth independent. Baroclinic effects are visible near the obstacle edge. If stratification is increased, the pressure perturbation becomes more and more bottom trapped whereas the surface elevation is reduced.

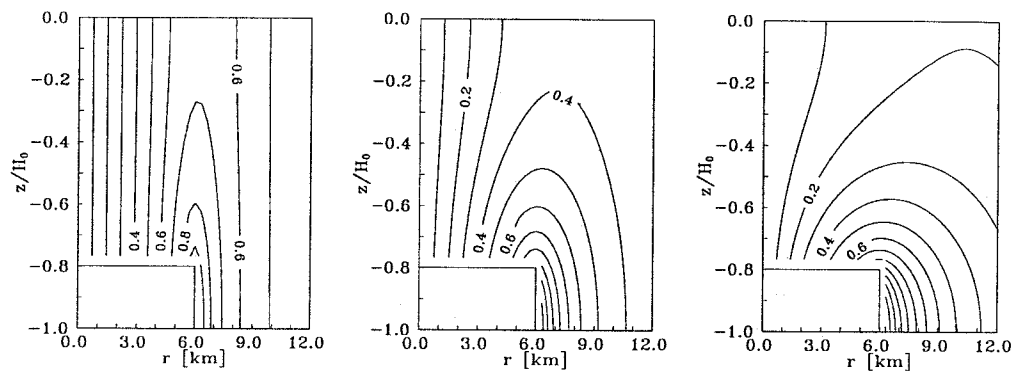


Figure 9: The baroclinic amplitude function  $\Gamma_{bk}(rz)$  according to eq. (2.126). The relative topographic height is 0.2, the obstacle radius is 6 km. The baroclinic Rossby radius is varied from 0.8 km (left), 2.1 km (middle) to 4 km (right).

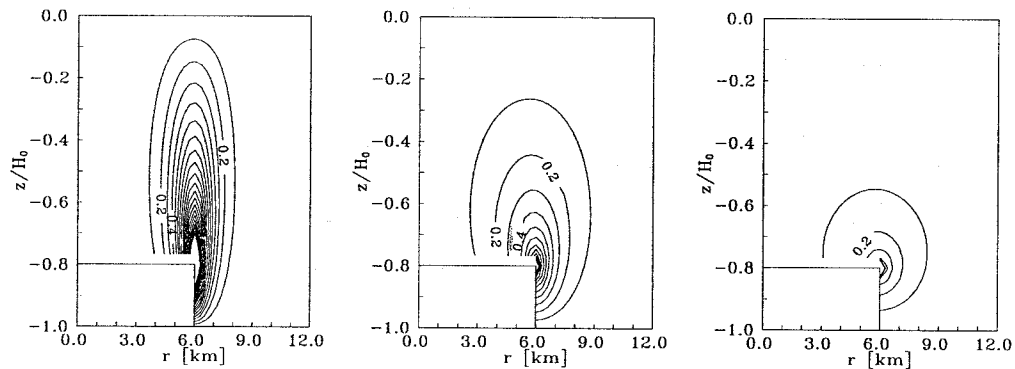


Figure 10: The displacement of isopycnals for several values of the baroclinic Rossby radius. The parameters are the same as in Fig. 9.

The baroclinic pressure perturbation corresponds to a vertical velocity

$$\tilde{w} = -\frac{1}{N^2}\psi_{zt}. \quad (2.127)$$

Within the linearized theory the above equation can be integrated to calculate the vertical displacement of isopycnals  $\Delta$ ,

$$\Delta = -\frac{1}{N^2}\psi_z. \quad (2.128)$$

There is also a barotropic contribution, since the derivative of the barotropic eigenfunction reads for constant Brunt Väisälä frequency

$$\frac{\partial}{\partial z} F_0(z) \approx -\frac{1}{\sqrt{H_0}} \frac{N^2}{g} \left(1 + \frac{z}{H_0}\right). \quad (2.129)$$

For  $z = 0$   $\Delta$  is the surface elevation. As shown in Fig. 10 the maximum displacement of isopycnals is found near the edge of the obstacle. The weaker the stratification is the more the displacement is concentrated near the obstacle edge whereas the amplitude of the displacement is increasing and the perturbation penetrates more to the surface. However, although  $\psi$  is a smooth function of  $z$  at  $z = -H_0 + h$  the vertical displacement at  $r = a$  is logarithmically divergent. This divergence does not vanish even for small stratification. The reason for this shortcoming is ambiguous. It may be either a consequence of the approximation made in the integral over the top of the obstacle. Alternatively it may result from the simple ansatz for the pressure at the sidewall which yields a concentration of all wave energy in a single topographic mode. Higher order approximations which possibly remove this singularity have not been tested.

### 3 Comparison with a numerical model

The analytical results are compared with the outcome of a free surface version of the GFDL-model. The details of the model implementation can be found in the report of KILLWORTH et al. (1989). The model is based on the nonlinear, hydrostatic Boussinesq equations and realized as a finite difference scheme on an Arakawa B-grid. The model topography was prepared with the same idealized shape as used in the analytical theory, i.e., a cylindrical obstacle of radius  $a$  and height  $h$  is placed in a homogeneous upstream flow. However, the steep obstacle sidewalls are simple approximations for an analytical treatment but a finite difference scheme may run in difficulties because of large vertical velocity values.

The numerical model includes nonlinear advective terms. These contributions could be removed to compare with the linear analytical results. However, since the model should be tested "as it is", linear conditions are established approximately by small values of the upstream flow. Choosing  $U_0 = 1 \text{ cm s}^{-1}$  the

typical time which is necessary to move a water particle over an obstacle of 20 km diameter is about 500 h and linear approximations are well justified.

Another problem is the treatment of friction. In analytical approaches the frictionless case is the most simple approximation, whereas friction is essential ingredient for the numerical stability of finite difference schemes. In the present experiments horizontally and vertically constant turbulent mixing coefficients are used. The model consists of a zonally periodic channel with  $300 \times 300$  horizontal grid points with a gridspacing of 1 km and 15 vertical levels of 2 m thickness. To keep the horizontal advection-diffusion scheme stable a minimum value of the vertical mixing coefficient of

$$A_H^{min} = 0.5u\Delta x \approx 5 \cdot 10^4 \text{cm}^2\text{s}^{-1} \quad (3.130)$$

is required. The vertical mixing coefficient should have the order of magnitude

$$A_V^{min} \approx \frac{\Delta z^2}{\Delta x^2} A_H^{min} \approx 2 \cdot 10^{-1} \text{cm}^2\text{s}^{-1}. \quad (3.131)$$

These values permit a maximum timestep of 240 s for the baroclinic mode and 12 s for the barotropic part of the model.

To initialize the homogeneous upstream flow a slight modification of the model code is necessary. In the beginning of the experiments a homogeneous barotropic flow  $U_0$  is set at all wet points. To prevent a spin down of the flow by lateral friction a small amount of momentum is added to the barotropic mode which exactly compensates the loss of momentum at the sidewalls. This small momentum correction can be calculated approximately from an analytical solution of the stationary barotropic momentum equation with lateral friction for a flat bottom. The flow correction vanishes everywhere with the exception of thin boundary layers at the sidewalls. Bottom friction is switched off. Then, in the central part of the flow where the obstacle is placed the upstream flow is homogeneously for a long time. For the timescales under consideration the flow perturbation remains trapped at the obstacle. The amplitude of the inertial waves irradiated from the obstacle is small and they do not interact with the obstacle via the periodic boundary conditions. Thus, the model setup reflects the same idealized boundary and initial conditions as in the analytical theory.

The model does not explode numerically as a consequence of the rough treatment in the initial time step. Due to the large ratio of the horizontal grid spacing to the vertical scale, the horizontal divergence of the flow is small even at the steep rise of the topography.

The first experiment concerns the case of weak stratification. The model runs with all baroclinic components but with constant salinity and only a small vertical gradient in the initial temperature field. The corresponding baroclinic Rossby radius of  $R_1 \approx 800$  m is not resolved by the model. The barotropic Rossby radius of 141 km is much larger than the obstacle radius of 20 km. The constant turbulent mixing coefficients for heat and salt are  $0.01 \text{ cm}^2\text{s}^{-1}$  for the vertical mixing and  $5 \cdot 10^4 \text{ cm}^2\text{s}^{-1}$  for the horizontal mixing. Several values for the relative height of the obstacle  $\frac{h}{H_0}$  have been tested. Fig. 11 is an example for  $\frac{h}{H_0} = 0.667$ . The time series of the surface elevation and the velocity field during the first orbit of the topographic wave round the obstacle is very similarly to the analytical result as shown in Fig. 4. The most obvious difference is the more pronounced enhancement of the flow over the seamount in the numerical experiment. For topography with smaller height the correspondence to the analytical result is improved. Fig. 12 shows numerical results from a model run with  $a > R_0$  corresponding to Fig. 6. To ensure numerical stability for the gridspacing of 8 km used in this experiment the horizontal mixing parameter has to be increased to  $A_H = 4 \cdot 10^5 \text{ cm}^2\text{s}^{-1}$ . Since in the first wave cycle strong inertial oscillations can be observed, the examples in Fig. 12 are taken from the second wave cycle.

If bottom friction is added, the topographic waves are damped and a stationary state is established after some time. A rough estimate for the equivalent friction constant  $\nu$  used in the numerical experiment is  $\nu \approx \frac{f}{50}$ . This is much smaller than the topographic frequency and the stationary flow velocity over the obstacle becomes very small. An example is shown in Fig. 13.

The topographic frequency can be estimated from time series of the angle of the zero line of the pressure perturbation with the upstream flow. Fig. 14 compares the topographic frequency as it follows from the numerical experiments in comparison with analytical results derived from the zeros of  $\sigma_{10}$ , eq. (2.76). The overall agreement is sufficient for seamounts with a radius much

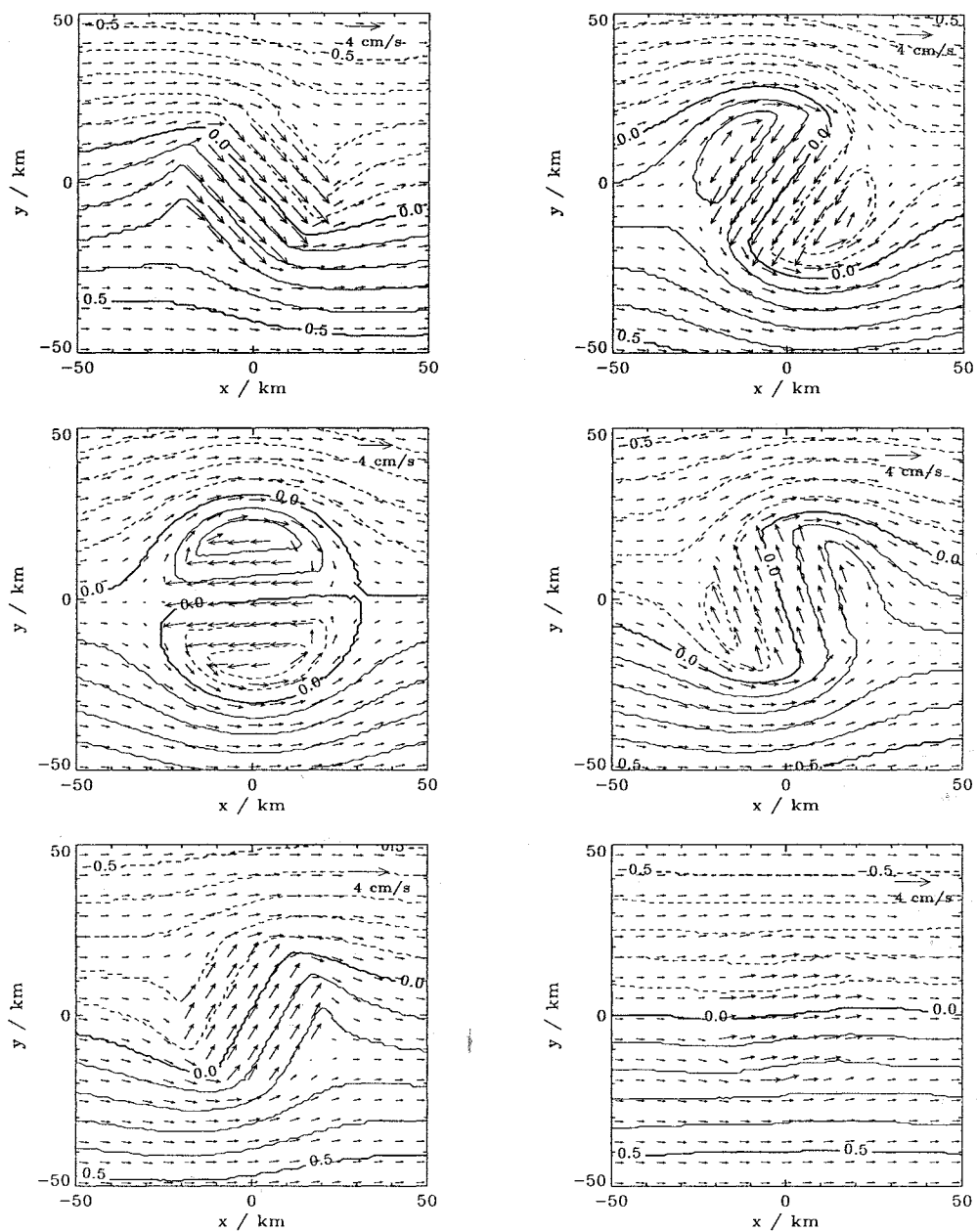


Figure 11: First cycle of the evolution of the topographic waves. The timesteps are 4h, 10h, 14h, 20h, 24h and 28h. The parameters are the same as in Fig. 4, a small viscosity is needed for numerical stability. The wave period is about 28.5h.

smaller than the barotropic Rossby radius but also for seamounts with a larger radius.

To make the numerical experiments with a baroclinic flow comparable with

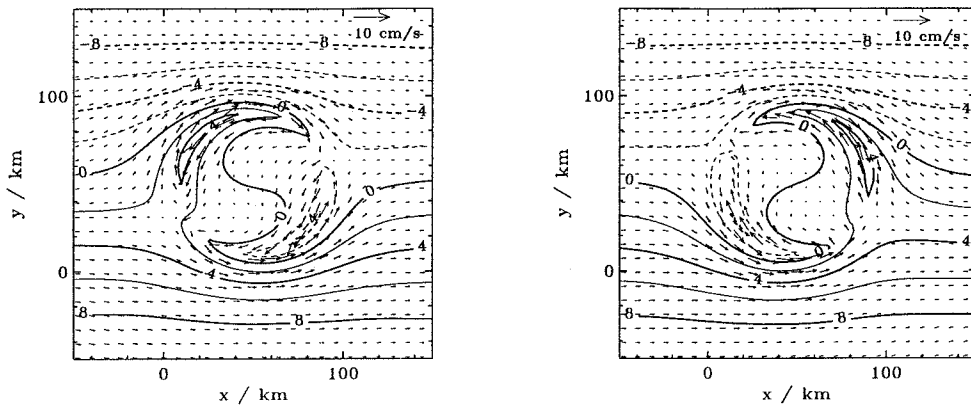


Figure 12: Surface elevation and flow field for  $t = 108h$  and  $t = 132h$ . The parameters are the same as in Fig. 6:  $\frac{h}{H_0} = 0.667$ , obstacle radius  $a = 320$  km,  $R_0 \approx 140$  km. The topographic frequency is  $\omega_{1b}^{topo} = 0.17f$ .

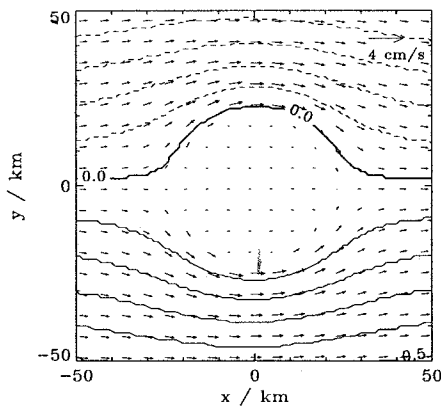


Figure 13: Stationary state controlled by friction for  $C_D \approx 0.007$ . The parameters are the same as in Fig. 4.

the analytical results of the previous section a linear vertical temperature and salinity profile has been chosen. As in the barotropic case the pressure perturbation is governed by one topographic wave clockwise encircling the obstacle. This supports the applicability of the iterative solution eq. (2.125) which allows for one topographic mode only. Contrary to the barotropic case the pressure perturbation is bottom intensified, the signal in the surface elevation

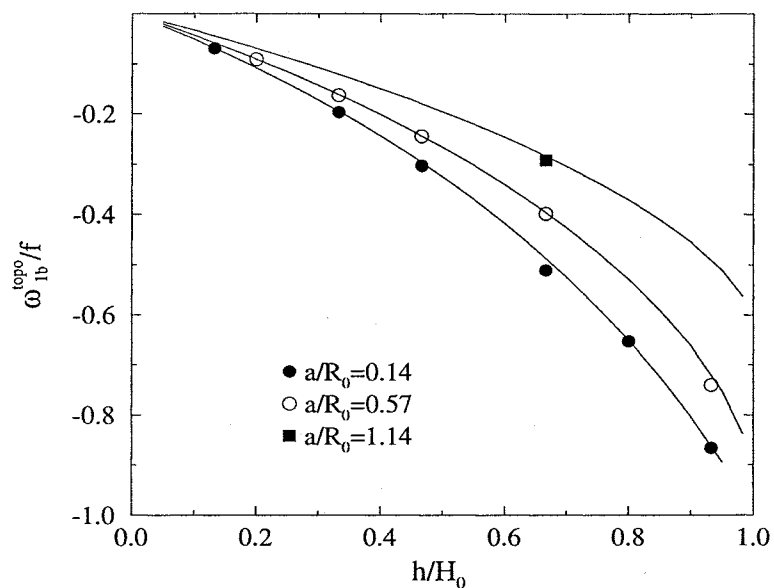


Figure 14: The analytically calculated wave spectrum, (—), and the results from the GFDL-model, ( $\bullet - \bullet$ ):  $\frac{a}{R_0} = 0.14$ , ( $\circ - \circ$ ):  $\frac{a}{R_0} = 0.57$ , ( $\blacksquare - \blacksquare$ ):  $\frac{a}{R_0} = 1.14$ . The barotropic Rossby radius is  $R_0 \approx 140$  km

is much weaker whereas internal up- and downwelling develops at the obstacle edges. The baroclinic signal is trapped horizontally within one baroclinic Rossby radius. Thus, stratification confines the pressure perturbation vertically and horizontally near the obstacle edge. Fig. 15 shows vertical sections of the temperature deviation from the stratification far upstream. Since the vertical temperature gradient is constant in the fluid at rest, the temperature deviation is proportionally to the vertical displacement of isopycnals and can be compared directly with Fig. 10. The enhanced bottom trapping with increasing stratification is obvious. The amount of the numerically calculated displacement of some dm is of the same order of magnitude as in the analytical theory.

Fig. 16 gives an example for one cycle of the topographic wave, which can be seen in the best way from the temperature perturbation immediately over the obstacle. The wave starts with upwelling upstream and downwelling downstream and finishes one cycle if the upwelling area has travelled towards

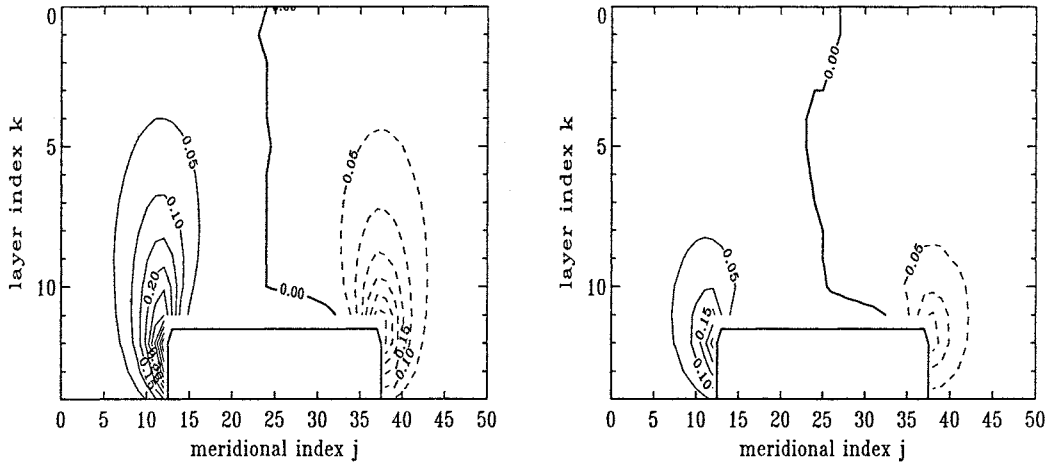


Figure 15: Vertical sections of the temperature deviation (in K) from the state of rest. The relative topographic height is 0.2, the obstacle radius is 6 km. The vertical salinity gradient is varied so that the baroclinic Rossby radius is 2.1 km (left) and 3.8 km (right). The displacement can be estimated approximately from the vertical temperature gradient,  $\frac{\Delta T}{\Delta z} = -0.25 \text{ K m}^{-1}$ .

the downstream side of the seamount.

Whereas in the analytical approach with small friction the pressure perturbation vanishes completely after one cycle, there is a small residual in the numerical experiments which stems possibly from nonlinear effects, friction, higher topographic modes and numerical effects as from the approximation of the cylindrical obstacle by a polygon in the model grid. Additionally, especially in the initial phase of the experiments inertial waves of small amplitude can be observed leaving the obstacle as spiraling waves. Another source of flow is the different vertical diffusion over and beside the obstacle which generates radial pressure gradients and a baroclinic circular flow with vertically changing orientation. However, here this effect is kept small by very small vertical mixing coefficients but it may drive flows of some  $\text{cm s}^{-1}$  in realistic models.

For a quantitative comparison of numerical and analytical results we consider the topographic frequency. Fig. 17 shows the relative frequency shift of the gravest topographic mode due to baroclinic effects as a function of

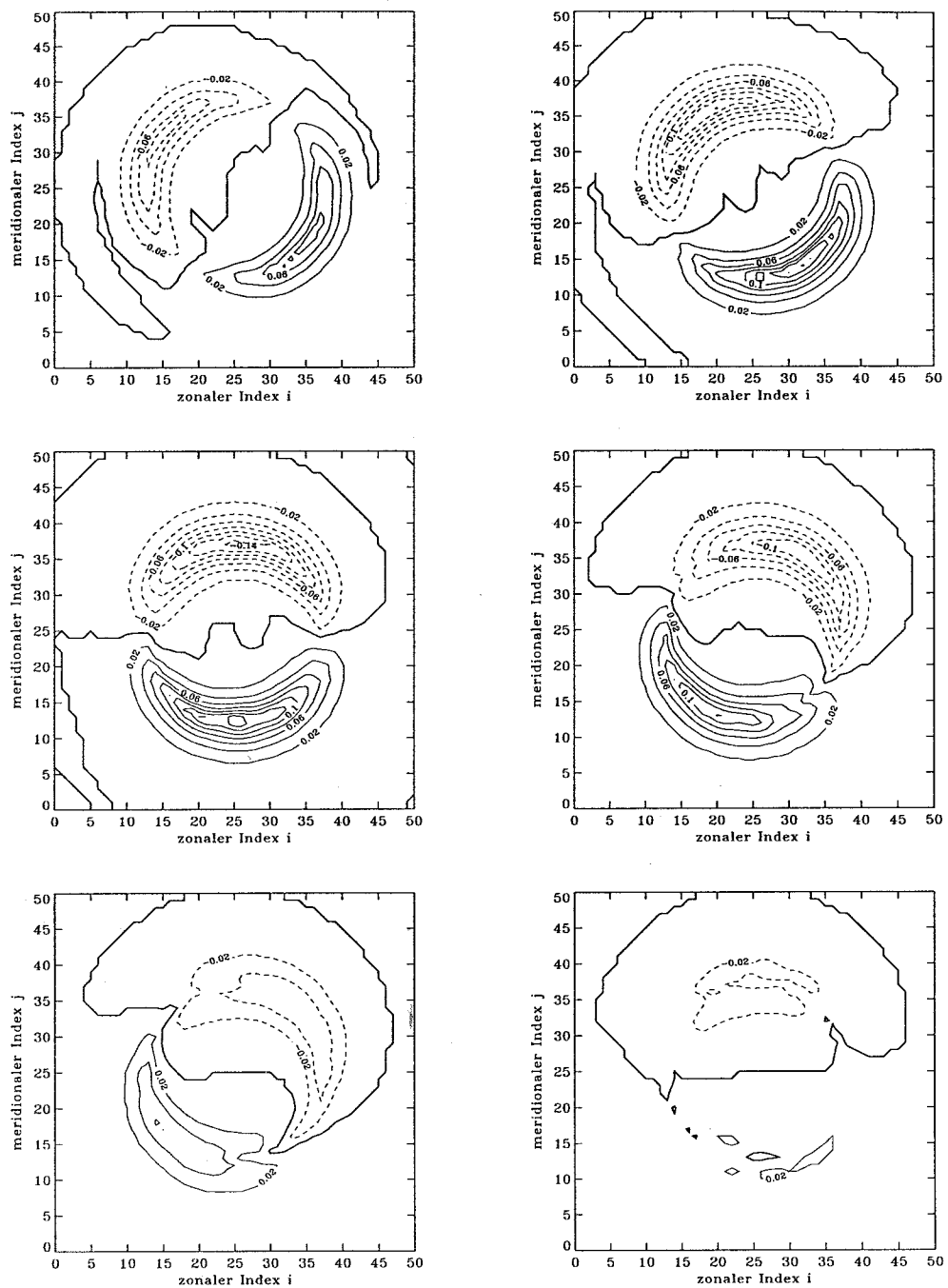


Figure 16: Series of snapshots representing the first cycle of a baroclinic topographic wave in equidistant time steps. The temperature deviation from the state of rest is shown. The obstacle radius: 12 km, relative height: 0.267, baroclinic Rossby radius: 2 km, wave period: 72 h

the relative topographic height. The analytical values are gained basing on

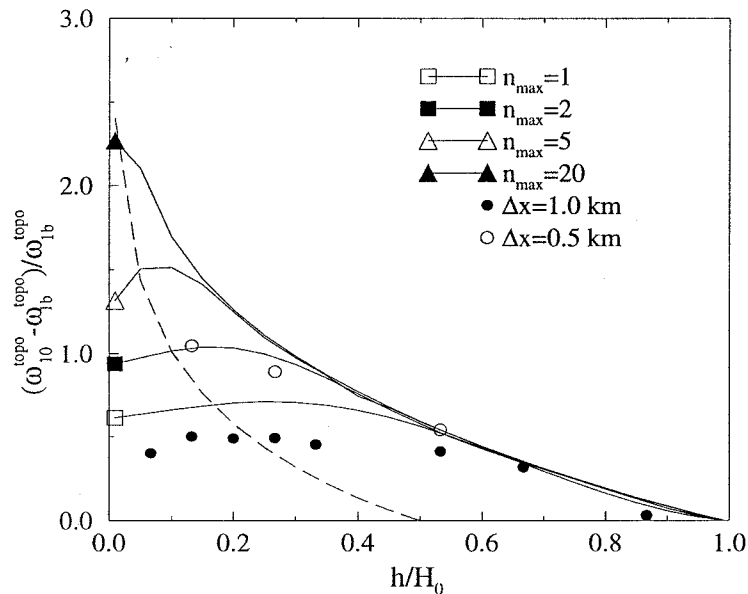


Figure 17: The relative frequency shift in the most prominent topographic mode due to baroclinic effects as function of the relative topographic height. The full lines, (—), stand for analytical results, the filled circles, ( $\bullet - \bullet$ ), for numerical model results with a horizontal grid spacing of  $\Delta x = 1$  km, the circles, ( $\circ - \circ$ ), for  $\Delta x = 0.5$  km. The barotropic Rossby radius is  $R_0 \approx 140$  km, the baroclinic Rossby radius  $R_1 \approx 2.1$  km, the obstacle radius  $a = 6$  km.

a decomposition of the pressure perturbation in vertical eigenfunctions, eq. (C.41). The different curves correspond to different levels of approximation, i.e. a varying number of vertical eigenfunctions is used. This illustrates the mode number dependence of the topographic frequency as discussed in section 2.5.2. In the analytical theory for high seamounts the mode coupling is weak and a small number of modes is sufficient to describe the pressure perturbation. For small seamounts strong mode coupling requires a large number of baroclinic modes. This picture is supported by the numerical experiments. Since the horizontal grid resolves only the first baroclinic Rossby radius the finite difference scheme suppresses strongly the higher vertical modes. Indeed, the values of the topographic frequency are close to the analytical approximation including only the first baroclinic vertical eigenfunction. Doubling the horizontal model resolution, i.e. resolving the second baroclinic Rossby radius, the

numerically determined frequency values are increased towards the analytical results including two vertical eigenfunctions.

## 4 Summary

The excitation of topographic waves at a cylindrical obstacle by a homogeneous flow has been studied by both, analytical calculations and numerical experiments. For conditions of small advection the analytical theory can start with the linearized Boussinesq equations. A Green function technique is used to derive perturbational solution methods. The solutions apply for seamounts of small height as well as for tall seamounts and islands. Both barotropic and baroclinic conditions have been investigated. For the barotropic case an exact solution can be found. If stratification is present, approximate solution techniques have been developed.

Within a homogeneous upstream flow suddenly switched on at  $t = 0$  topographic waves trapped at the obstacle edge can be observed. The perturbation of the pressure field has dipole form and encircles the obstacle clockwise (in the northern hemisphere). In all cases under consideration one topographic wave mode is dominating. If the obstacle radius is small compared to the barotropic Rossby radius the wave frequency is proportionally to the inertial frequency and to the relative topographic height  $\frac{h}{H_0}$ . The topographic wave frequency decreases with increasing obstacle radius. Stratification leads to an enhancement of the topographic frequency.

The analytical results are compared with numerical experiments based on the GFDL-model. In the barotropic case the analytically calculated and the numerically gained topographic frequency agree excellently. If stratification is present, there is good correspondence of both approaches for tall seamounts but a discrepancy for small obstacles. This can be traced back to the limited horizontal resolution of the numerical model suppressing higher baroclinic partial waves which are necessary to compose the topographic wave modes. However, this is a minor shortcoming since at obstacles of small height the wave period is much larger than the inertial period and other processes may destroy the waves quickly. The influence of the finite grid spacing on the

amount of internal upwelling has not been investigated.

In most the examples considered the flow is in geostrophic balance with the pressure gradients, ageostrophic components as inertial oscillations are of some importance only in the initial phase of the experiment and for obstacles with a radius comparable with the barotropic Rossby radius. Even when the flow is controlled by friction, the geostrophic flow components dominate. By friction the flow perturbation at the obstacle becomes stationary. Contrary to Taylor columns the production of vorticity is balanced by dissipation. If friction is small, the flow over the obstacle vanishes approximately. Especially in shallow seas the flow variability is too high to allow for the observation of these stagnant conditions in nature, but as a tendency an influence on material transport and sedimentation is expected.

The analytical results are easy to implement on a PC and may give a quick orientation on the spectrum of topographic waves near obstacles. Although the results correspond to idealized conditions the comparison with the numerical model shows that major properties are well described. Improvements of the theory are possible. Using the homogeneous upstream flow as the reference state for linearizing the basic equations, a quasi-linear theory can be derived which includes the damping of topographic waves due to advection. Horizontal and vertical turbulent mixing as well as bottom friction may be discussed separately and in more detail. However, this would make the analytical equations intractable and a numerical investigation should be preferred.

## A The approximation of weak stratification

We consider the limit  $N^2 \rightarrow 0$  or equivalently  $\alpha_1 \rightarrow \infty$ . Using the asymptotic representation for the modified Bessel functions  $K_m$  and  $I_m$  the baroclinic components of the Green function are

$$g_{mn}(rr') \approx \frac{\theta(r-r')e^{\alpha_n(r'-r)} + \theta(r'-r)e^{\alpha_n(r-r')}}{2\alpha_n\sqrt{rr'}}, \quad (\text{A.1})$$

i.e., the baroclinic part of the Green function vanishes for weak stratification.

The first term in eq. (2.61)

$$\psi_m^t(rz\omega) = - \int_0^a dr' r' \psi_m(r'z'\omega) \frac{f^2 - \omega^2}{N^2} \frac{\partial}{\partial z'} L_m(rzr'z'\omega) \Big|_{z'=-H_0+h} \quad (\text{A.2})$$

is proportionally to  $N^{-2}$  and has to be considered separately. We consider the barotropic and the baroclinic part of the Green function separately. This is possible since the Green function corresponds to the flat bottom case and can be decomposed naturally into vertical eigenfunctions  $F_n$ . We use the identity

$$\begin{aligned} \frac{f^2 - \omega^2}{N^2} \frac{\partial}{\partial z} F_n(z) \Big|_{z=-H_0+h} &= \int_{-H_0}^{-H_0+h} dz Z F_n(z) \\ &= - \int_{-H_0}^{-H_0+h} dz \alpha_n^2 F_n(z). \end{aligned} \quad (\text{A.3})$$

The integrand of the baroclinic part in eq. (A.2) is different from zero only in a small area round the point  $r' = r$ . Thus, the  $r'$  integration can be carried out,

$$\begin{aligned} \psi_m^t(rz\omega) &\approx - \frac{h}{H_0} \int_0^a dr' r' \psi_m(r', -H_0 + h, \omega) \frac{f^2 - \omega^2}{f^2 R_0^2} g_m(rr'\omega) \\ &\quad - \theta(a-r) \sum_{n>0} \int_{-H_0}^{-H_0+h} dz' F_n(z) F_n(z') \psi(r, -H_0 + h, \omega). \end{aligned} \quad (\text{A.4})$$

By the completeness of the eigenfunctions  $F_n$  the sum can be performed and the barotropic approximation for  $\psi^t$  reads

$$\begin{aligned} \psi_m^t(rz\omega) &\approx - \frac{h}{H_0} \int_0^a dr' r' \psi_m(r', -H_0 + h, \omega) \frac{f^2 - \omega^2}{f^2 R_0^2} g_m(rr'\omega) \\ &\quad - \theta(a-r) \psi(r, -H_0 + h, \omega) \left( \theta(-z - H_0 + h) - \frac{h}{H_0} \right). \end{aligned} \quad (\text{A.5})$$

Never stepping into the bottom  $\psi^i$  is independent of  $z$  and the barotropic equation reads

$$\begin{aligned} \psi_{m0}(r\omega) = & -\frac{h}{H_0} \left( \int_0^a dr' r' \psi_{m0}(r'\omega) \frac{f^2 - \omega^2}{f^2 R_0^2} g_{m0}(rr'\omega) - \theta(a-r) \psi_{m0}(r\omega) \right. \\ & \left. + i \frac{f^2 - \omega^2}{\omega} u^0 \pi a \delta_{|m|,1} g_{m0}(ra\omega) - \mathcal{G}_{m0}(ra\omega) \psi_{m0}(a\omega) \right). \end{aligned} \quad (\text{A.6})$$

## B Exact solution of the barotropic equation

The barotropic equation for  $r < a$ , i.e. in the area over the topography, reads

$$\begin{aligned} \psi_{m0}^i(r\omega) = & C \tilde{h} I_m(\alpha_0 r) \\ & - \tilde{h} \alpha_0^2 \int_0^r dr' r' \psi_{m0}^i(r'\omega) I_m(\alpha_0 r') K_m(\alpha_0 r) \\ & + \tilde{h} \alpha_0^2 \int_r^a dr' r' \psi_{m0}^i(r'\omega) I_m(\alpha_0 r) K_m(\alpha_0 r') \end{aligned} \quad (\text{B.1})$$

where

$$\begin{aligned} \tilde{h} &= \frac{h}{H_0 - h} \\ C &= -C_u K_m(\alpha_0 a) \\ &+ \left( -a \alpha_0 K_{m+1}(\alpha_0 a) + m \left( 1 - \frac{f}{\omega} \right) K_m(\alpha_0 a) \right) \psi_{m0}(a\omega). \end{aligned} \quad (\text{B.2})$$

The subscript 0 mean barotropic approximation. This equation is solved by the ansatz

$$\psi_{m0}^i(r\omega) \sim I_m(\beta r). \quad (\text{B.3})$$

All integrals can be performed analytically,

$$\psi_{m0}^i(r\omega) = \tilde{h} C I_m(\beta r) D_{m0}^{-1}, \quad (\text{B.4})$$

$$D_{m0} = a \beta I_{|m|+1}(\beta a) K_m(\alpha_0 a) + a \alpha_0 I_m(\beta a) K_{|m|+1}(\alpha_0 a), \quad (\text{B.5})$$

$$\beta^2 = \alpha_0^2 \frac{H_0}{H_0 - h}. \quad (\text{B.6})$$

At  $r = a$   $\psi$  reads

$$\psi_{m0}(a\omega) = \frac{-\frac{h}{H_0} C_u K_m(\alpha_0 a) I_m(\beta a) D_{m0}^{-1}}{\sigma_{m0}(\omega)}. \quad (\text{B.7})$$

The denominator

$$\begin{aligned} \sigma_{m0}(\omega) = & 1 - \frac{h}{H_0} \\ & - \frac{h}{H_0} \left( -a\alpha_0 K_{m+1}(\alpha_0 a) + m \left( 1 - \frac{f}{\omega} \right) K_m(\alpha_0 a) \right) I_m(\beta a) D_{m0}^{-1} \end{aligned} \quad (\text{B.8})$$

determines the spectrum of  $\psi$ . The complete solution over the topography is

$$\psi_{m0}^i(r\omega) = \frac{-\frac{h}{H_0} C_u K_m(\alpha_0 a) I_m(\beta r) D_{m0}^{-1}}{\sigma_{m0}(\omega)}. \quad (\text{B.9})$$

Inserting this result in the pressure equation for  $r > a$  it follows

$$\psi_{m0}^a(r\omega) = \frac{-\frac{h}{H_0} C_u K_m(\alpha_0 r) I_m(\beta a) D_{m0}^{-1}}{\sigma_{m0}(\omega)}. \quad (\text{B.10})$$

## C The baroclinic approximation

With the ansatz

$$\psi_m^i(r\omega) = \psi_m^i(a\omega) \frac{I_m(\beta r)}{I_m(\beta a)} \quad (\text{C.1})$$

an baroclinic approximation for  $\psi_m^t$  (A.2) can be found. The  $r'$  integral can be performed analytically. For the pressure perturbation over and beside the obstacle it follows an integral equation in terms of  $z$ ,

$$\begin{aligned} \psi_m^i(rz\omega) \approx & - \int_{-H_0}^{-H_0+h} dz' \sum_n F_n(z) F_n(z') \\ & \left( \psi_m^i(a, -H_0 + h) \frac{\alpha_n^2}{\beta^2 - \alpha_n^2} \frac{I_m(\alpha_n r) D_{mn} - I_m(\beta r)}{I_m(\beta a)} \right. \\ & \left. + C_u g_{mn}^<(ra) - \mathcal{G}_{mn}^<(ra) \psi_m^a(az'\omega) \right) \end{aligned} \quad (\text{C.2})$$

$$\begin{aligned} \psi_m^a(rz\omega) \approx & - \int_{-H_0}^{-H_0+h} dz' \sum_n F_n(z) F_n(z') \\ & \left( \psi_m^i(a, -H_0 + h) \frac{\alpha_n^2}{\beta^2 - \alpha_n^2} \right. \\ & \left. \frac{K_m(\alpha_n r) \left( \beta a I_{|m|+1}(\beta a) I_m(\alpha_n a) - \alpha_n a I_m(\beta a) I_{|m|+1}(\alpha_n a) \right)}{I_m(\beta a)} \right. \\ & \left. + C_u g_{mn}^>(ra) - \mathcal{G}_{mn}^>(ra) \psi_m^a(az'\omega) \right) \end{aligned} \quad (\text{C.3})$$

$D_{mn}$  is the direct generalization of  $D_{m0}$  in Appendix B.

$\psi$  is a smooth function at both  $z = -H_0 + h$  and  $r = a$ . To show this, we consider the matching condition of the inner and the outer solution at  $r = a$ ,

$$\psi_m^a(az\omega) - \psi_m^i(az\omega) = \int_{-H_0}^{-H_0+h} dz' \sum_n F_n(z) F_n(z') \psi_m^a(az'\omega). \quad (\text{C.4})$$

which follows from the relation

$$\mathcal{G}_{mn}^>(aa) - \mathcal{G}_{mn}^<(aa) = 1 \quad (\text{C.5})$$

as well as from the analytical properties of the modified Bessel function. Above the level  $z > -H_0 + h$   $\psi$  is a continuous function at  $r = a$  whereas below that level there is a step in  $\psi$  at the sidewall of the obstacle. This follows from the completeness of the eigenfunctions,

$$\sum_n F_n(z) F_n(z') = \delta(z - z'), \quad (\text{C.6})$$

i.e., the right hand side of eq. (C.4) becomes zero for  $z > -H_0 + h$ .

The behavior of  $\psi_m^a$  at  $z = -H_0 + h$  can be derived analytically in the limit  $R_1 \rightarrow 0$ . The lowest order in  $R_1$  is

$$\begin{aligned} \psi_m^a(rz\omega) \approx & - \int_{-H_0}^{-H_0+h} dz' \sum_{n>0} F_n(z) F_n(z') \\ & \sqrt{\frac{a}{4r}} e^{\alpha_n(a-r)} \left( \psi_m^i(a, -H_0 + h) - \psi_m^a(az'\omega) \right) \\ & + \text{barotropic terms.} \end{aligned} \quad (\text{C.7})$$

(Note, that this approximation is valid only if  $\beta^2 \ll \alpha_n^2$ , in the near island case some baroclinic modes have to be treated separately!). The higher order terms converge as  $n^{-2}$ . From the completeness of the eigenfunctions it follows that the above expression is smoothly even for  $r = a$ .

The integral equation (C.3) for  $\psi_m^a(r, z, \omega)$  can be solved in two steps. The first step is the solution for  $r = a$ . Since  $\psi_m^a(z)$  is smoothly at  $z = -H_0 + h$  it has not to be specified whether the point  $z = -H_0 + h + \delta$  or  $z = -H_0 + h - \delta$  is considered. Using the equation for  $\psi_m^i$  one has to consider the point above the top of the obstacle, i.e.  $z = -H_0 + h + \delta$ , and not to step into the bottom. As the next step the solution  $\psi_m^a(az\omega)$  is reinserted into eq. (C.3) to get the complete solution.

The integral equation for  $\psi_m(az\omega)$  reads

$$\begin{aligned} \psi_m(az\omega) \approx & - \int_{-H_0}^{-H_0+h} dz' \sum_n F_n(z) F_n(z') \left( C_u g_{mn}^>(aa) \right. \\ & + \psi_m(a, -H_0 + h) \frac{\alpha_n^2}{\beta^2 - \alpha_n^2} \left( \frac{I_m(\alpha_n a) D_{mn}}{I_m(\beta a)} - 1 \right) \\ & \left. - \mathcal{G}_{mn}^>(aa) \psi_m(az'\omega) \right) \end{aligned} \quad (\text{C.8})$$

To avoid the occurrence of slowly converging sums the above equation has to be rearranged. From the asymptotic result for large  $n$

$$I_m(\alpha_n a) K_{m+1}(\alpha_n a) \alpha_n a \rightarrow \frac{1}{2} \quad (\text{C.9})$$

it follows that there are sums converging very slowly as the power series of a step like function. Separating these terms the above equation can be rewritten in such a way that all series converge at least as  $n^{-2}$ . Additionally,  $\psi_m(a, -H_0 + h)$  is eliminated and the resulting equation for  $\psi_m(az\omega)$  looks much more complicated but is suitable for a perturbational treatment since all contributions are well defined convergent sums,

$$\begin{aligned} \psi_m(z) \left( 1 - \frac{1}{2} \theta(h - H_0 - z) \right) = & \psi_m^0(z) - \psi_m^0 \frac{A(z) + \frac{1}{2} \theta(h - H_0 - z)}{1 + A} \\ & - \sum_n \int_{-H_0}^{-H_0+h} dz' F_n(z') B_n \psi_m(z') \left( F_n(z) - F_n \frac{A(z) + \frac{1}{2} \theta(h - H_0 - z)}{1 + A} \right) \end{aligned} \quad (\text{C.10})$$

with the functions

$$\begin{aligned} \psi_m^0(z) &= - \int_{-H_0}^{-H_0+h} dz' \sum_n F_n(z) F_n(z') C_u g_{mn}^>(aa\omega) \quad (\text{C.11}) \\ A(z) &= \int_{-H_0}^{-H_0+h} dz' \sum_n F_n(z) F_n(z') A_n \\ A_n &= \left( \frac{\alpha_n^2}{\beta^2 - \alpha_n^2} \left( \frac{I_m(\alpha_n a) D_{mn}}{I_m(\beta a)} - \frac{1}{2} \right) - \frac{1}{2} \frac{\beta^2}{\beta^2 - \alpha_n^2} \right) \\ B_n &= -\frac{1}{2} + \alpha_n a I_m(\alpha_n a) K_{m+1}(\alpha_n a) \\ &\quad - m \left( 1 - \frac{f}{\omega} \right) I_m(\alpha_n a) K_m(\alpha_n a). \end{aligned} \quad (\text{C.12})$$

The functions  $A$ ,  $\psi^0$  and  $F_n$  without arguments denote the function value at  $z = -H_0 + h$ .

## C.1 Solution by iteration

The integrand at the right hand side of eq. (C.3) has its maximum value at  $z' = z$ . Thus, as a first order approximation  $\psi_m^a$  under the integral is replaced by the constant value

$$\psi_m(az'\omega) \approx \psi_m(a, -H_0 + h, \omega). \quad (\text{C.13})$$

This approximation will be excellent in the near barotropic case and for topography of small relative height.

The result is a closed equation for  $\psi_m^a(a, -H_0 + h\omega)$ . The solution reads

$$\psi_m(-H_0 + h) = \frac{\psi_m^0(-H_0 + h)}{1 + \int_{-H_0}^{-H_0+h} dz' \sum_n F_n(-H_0 + h) F_n(z') (A_n + B_n)}. \quad (\text{C.14})$$

The topographic frequency follows from the zeros in the denominator of eq. (C.14). Resolving for  $\omega$  the topographic frequency reads

$$\omega_m^{\text{topo}} \approx -f \frac{m \int_{-H_0}^{-H_0+h} dz' \sum_n F_n(-H_0 + h) F_n(z') I_m(\alpha_n a) K_m(\alpha_n a)}{1 + \int_{-H_0}^{-H_0+h} dz' \sum_n F_n(-H_0 + h) F_n(z') Q_n}, \quad (\text{C.15})$$

$$Q_n = \frac{\alpha_n^2}{\beta^2 - \alpha_n^2} \left( \frac{I_m(\alpha_n a)}{I_m(\beta a)} D_{mn} - 1 \right) - \alpha_n a K_m(\alpha_n a) I_{m+1}(\alpha_n a) - m I_m(\alpha_n a) K_m(\alpha_n a). \quad (\text{C.16})$$

Eq. (C.15) can be evaluated numerically. An analytical result can be found for  $\alpha_0 a \ll 1$  and  $\alpha_1 a \gg 1$ . As shown for the barotropic case the topographic frequency is much smaller than  $f$  for  $h \ll H_0$ . Then, the right hand side of eq. (C.15) becomes independent of  $\omega$  with the approximation

$$\alpha_n a \approx \frac{a}{R_n}. \quad (\text{C.17})$$

A selfconsistent solution may be of some interest for the weakly stratified case, where the assumption  $\psi_m(az'\omega) \approx \psi_m(a, -H_0 + h, \omega)$  is justified for high seamounts also.

For the modified Bessel functions the approximations

$$I_n(\alpha_n a) K_m(\alpha_n a) \approx \begin{cases} \frac{1}{2|m|} + \mathcal{O}((\alpha_0 a)^2) & \text{for } n = 0, \\ \frac{1}{2\alpha_n a} + \mathcal{O}((\alpha_n a)^{-2}) & \text{for } n \geq 1, \end{cases} \quad (\text{C.18})$$

are valid and  $Q_n$  reads approximately

$$Q_n \approx \begin{cases} -\frac{1}{2} + \mathcal{O}(\alpha_0^2 a^2) & \text{for } n = 0, \\ -\frac{|m|}{2\alpha_n a} + \mathcal{O}\left(\frac{\alpha_0^2 a^2}{\alpha_n a}\right) & \text{for } n \geq 1 \end{cases} \quad (\text{C.19})$$

It is independent of  $h$ . If the Brunt Väsiälä frequency is constant, the vertical eigenfunctions are

$$F_0(z) = \frac{1}{\sqrt{H_0}} \quad (\text{C.20})$$

$$F_n(z) = (-1)^n \sqrt{\frac{2}{H_0}} \cos\left(\frac{n\pi z}{H_0}\right). \quad (\text{C.21})$$

The  $z'$  integral can be performed.

$$F_n(-H_0 + h) \int_{-H_0}^{-H_0+h} dz' F_n(z') = \begin{cases} \frac{h}{H_0} & \text{for } n = 0, \\ \frac{1}{n\pi} \sin\left(\frac{2n\pi h}{H_0}\right) & \text{for } n \geq 1 \end{cases} \quad (\text{C.22})$$

The topographic frequency reads with the above approximations for  $Q_n$

$$\omega_m^{\text{topo}} \approx -f \frac{\text{sgn}(m) \frac{h}{2H_0} + \frac{m}{2\pi\alpha_1 a} \mathcal{C}\left(\frac{2\pi h}{H_0}\right)}{1 - \frac{h}{2H_0} - \frac{|m|}{2\pi\alpha_1 a} \mathcal{C}\left(\frac{2\pi h}{H_0}\right)}. \quad (\text{C.23})$$

The sum

$$\mathcal{C}(x) = \sum_{n \geq 1} \frac{\sin(nx)}{n^2} \quad (0 \leq x \leq \pi) \quad (\text{C.24})$$

denotes Clausen's integral. For  $x < \frac{\pi}{2}$ , i.e.  $\frac{h}{H_0} \leq \frac{1}{4}$ , it reads approximately

$$\mathcal{C}(x) \approx x(1 - \ln(x)). \quad (\text{C.25})$$

The spatial structure of the pressure perturbation follows if eq. (C.14) is reinserted at the right hand in eq.s (C.2) and (C.3) as an approximation of  $\psi(az'\omega)$ . In the most cases the barotropic Rossby radius is much larger than the baroclinic Rossby radius,  $R_0 \gg R_1$ , and the approximation

$$\frac{\alpha_n^2}{\beta^2 - \alpha_n^2} \approx \begin{cases} \frac{H_0 - h}{h} & \text{for } n = 0, \\ -1 & \text{for } n \geq 1. \end{cases} \quad (\text{C.26})$$

permits a considerable simplification. With the Wronskian of the modified Bessel functions,

$$I_{m+1}(x)K_m(x) + K_{m+1}(x)I_m(x) = \frac{1}{x}, \quad (\text{C.27})$$

the pressure perturbation can be written as

$$\psi_m^i(rz\omega) \approx C_u \bar{\omega} \frac{\omega_m^{topo}}{fm} \frac{(I_m(\beta r) - I_m(\alpha_0 r) D_{m0}) \mathcal{L}_m^<(a, -H_0 + h) + I_m(\alpha_0 a) D_{m0} \mathcal{L}_m^<(rz)}{\mathcal{L}_m(a, -H_0 + h) I_m(\beta a) (\bar{\omega} - \omega_m^{topo})}, \quad (C.28)$$

$$\begin{aligned} \psi_m^a(rz\omega) \approx C_u \bar{\omega} \frac{\omega_m^{topo}}{fm} & \left[ \mathcal{L}_m^>(rz) + \left( \frac{I_{m+1}(\beta a)}{I_m(\beta a)} \beta a I_m(\alpha_0 a) - \alpha_0 a I_{m+1}(\alpha_0 a) \right) \right. \\ & \left. (\mathcal{L}_m^>(rz) K_m(\alpha_0 a) - \mathcal{L}_m^>(a, -H_0 + h) K_m(\alpha_0 r)) \right] / \\ & \left[ \mathcal{L}_m(a, -H_0 + h) (\bar{\omega} - \omega_m^{topo}) \right], \end{aligned} \quad (C.29)$$

with

$$\mathcal{L}_m^{\gtrless}(rz) = \sum_n \int_{-H_0}^{-H_0+h} dz' F_n(z') F_n(z) g_{mn}^{\gtrless}(ra). \quad (C.30)$$

For consistency the topographic frequency has to be calculated on the same level of approximation as  $\psi$ ,

$$\omega_m^{topo} \approx -fm \frac{\mathcal{L}_m(a, -H_0 + h)}{\frac{I_m(\alpha_0 a)}{I_m(\beta a)} D_{m0} - \left( \frac{I_{m+1}(\beta a)}{I_m(\beta a)} \beta a + m \right) \mathcal{L}_m(a, -H_0 + h)}. \quad (C.31)$$

For small topography, i.e.  $\beta = \alpha_0$ , the above result may be simplified to

$$\psi_m^{a/i}(rz\omega) \approx \frac{C_u \bar{\omega} \omega_m^{topo}}{fm} \frac{\mathcal{L}_m^{\gtrless}(rz)}{\mathcal{L}_m(a, -H_0 + h) (\bar{\omega} - \omega_m^{topo})}, \quad (C.32)$$

with

$$\omega_m^{topo} \approx -fm \frac{\mathcal{L}_m(a, -H_0 + h)}{1 - \left( \frac{I_{m+1}(\alpha_0 a)}{I_m(\alpha_0 a)} \alpha_0 a + m \right) \mathcal{L}_m(a, -H_0 + h)}. \quad (C.33)$$

## C.2 Decomposition into vertical eigenfunctions

The perturbational result as given in the previous appendix C.1 filters out only one mode of the topographic waves. Eq. (C.10) can be decomposed into

vertical eigenfunctions. Multiplying with an eigenfunction  $F_n$  and integrating over the interval  $(-H_0, -H_0 + h)$  the following matrix equation is obtained

$$\psi_n = I_n + \sum_l T_{nl} \psi_l. \quad (\text{C.34})$$

The inhomogeneity  $I_n$  depends on  $\psi^0$ ,

$$I_n = 2\psi_n^0 - \frac{\psi^0}{(1+A)F_0} \left( M_{0n} + 2 \sum_k M_{nk} M_{k0} A_k \right) \quad (\text{C.35})$$

the matrix  $T_{nl}$  reads

$$T_{nl} = \frac{B_l F_l}{(1+A)F_0} \left( M_{0n} + 2 \sum_k M_{nk} M_{k0} A_k \right) - 2M_{nl} B_l \quad (\text{C.36})$$

with

$$\psi_n = \int_{-H_0}^{-H_0+h} dz F_n(z) \psi(z), \quad (\text{C.37})$$

$$M_{nl} = \int_{-H_0}^{-H_0+h} dz F_n(z) F_l(z), \quad (\text{C.38})$$

$$F_n = F_n(-H_0 + h). \quad (\text{C.39})$$

The angular index  $m$  has been suppressed to avoid confusion with the vertical mode numbers. The other quantities are defined in eq. (C.12).

For constant Brunt Väisälä frequency the matrix  $M_{nl}$  reads

$$M_{nl} = \begin{cases} \frac{h}{H_0} & \text{for } n = 0, l = 0 \\ \frac{\sqrt{2}}{n\pi} \sin\left(\frac{n\pi h}{H_0}\right) & \text{for } n = 0, l \geq 1 \\ \frac{h}{H_0} + \frac{1}{2n\pi} \sin\left(\frac{2n\pi h}{H_0}\right) & \text{for } n = l \geq 1 \\ \frac{1}{\pi} \left( \frac{\sin\left(\frac{(n-l)\pi h}{H_0}\right)}{n-l} + \frac{\sin\left(\frac{(n+l)\pi h}{H_0}\right)}{n+l} \right) & \text{for } n, l \geq 1 \end{cases} \quad (\text{C.40})$$

The set of equations (C.35) is of rank  $\infty$ . Since  $T_{nl}$  is a diagonal matrix in the island case truncation of the sums at some maximum value  $n_{max}$  does not influence the result for the modes included. Thus, the approximation of the infinite set (C.35) by a finite number of equations is a good approximation for high seamounts.

The spectrum defined by the zeros of the determinant of the homogeneous system of equations,

$$\text{Det}(1 - \hat{T}) = 0. \quad (\text{C.41})$$

## Acknowledgement

I would like to thank Prof. W. Fennel and Dr. T. Seifert for stimulating discussions as well as B. Kayser for technical assistance. This work was supported by the BMBF, project 03F0076A.

## References

- ABRAMOWITZ, M., STEGUN, I. A., 1984: *Handbook of Mathematical Functions*. Verlag Harri Deutsch, Thun-Frankfurt.
- ARFKEN, G., 1970: *Mathematical methods for physicists*. Academic Press, New York, London.
- BECKMANN, A., HAIDVOGEL, D. B., 1993: Numerical simulation of flow around a tall isolated seamount. part i: Problem formulation and model accuracy. *Journal of Physical Oceanography*, **23**, 1736–1753.
- BRINK, K. H., 1989: The effect of stratification on seamount-trapped waves. *Deep-Sea Research*, **36**, 825–844, 1989.
- DAVEY, M. K., HURST R. G. A., JOHNSON, E. R., 1993: Topographic eddies in a multilayer flow. *Dynamics of Atmospheres and Oceans*, **18**, 1–27.
- FENNEL, W., SCHMIDT, M., 1991: Responses to topographic forcing. *Journal of Fluid Mechanics*, **223**, 209–240.
- FOSTER, M. R., 1989: Rotating stratified flow past a steep-sided obstacle. incipient separation. *Journal of Fluid Mechanics*, **206**, 47–73.
- GJEVIK, B., MOE, H., 1994: Steady and transient flows around banks located near a shelf edge. *Continental Shelf Research*, **14**, 1389–1409.
- HAIDVOGEL, D. B., BECKMANN, A., LIN, R.-Q., 1993: Numerical simulation of flow around a tall isolated seamount. part ii: Resonant generation of trapped waves. *Journal of Physical Oceanography*, **23**, 2373–2391.
- HICKIE, B. P., 1972: Taylor columns for small rossby numbers. In *Proceedings of the GFD Summer School*, volume II, pages 29–39.
- HOGG, N. G., 1973: On the stratified taylor column. *Journal of Fluid Mechanics*, **58**, 517–537.
- HUPPERT, H. E., 1975: Some remarks on the initiation of inertial taylor columns. *Journal of Fluid Mechanics*, **67**, 397–412.

- HUPPERT, H. E., BRYAN, K., 1976: Topographically generated eddies. *Deep-Sea Research*, **23**:655-679.
- HUTHNANCE, J. M., 1974: On the diurnal tidal currents over rockall bank. *Deep-Sea Research*, **21**, 23-35.
- INGERSOLL, A. P., 1969: Inertial taylor columns and jupiters great red spot. *Journal of Atmospheric Sciences*, **26**, 744-752.
- JAMES, I. N., 1980: The forces due to geostrophic flow over shallow topography. *Geophysical and Astrophysical Fluid Dynamics*, **14**, 225-250.
- JOHNSON, E. R., 1984: Starting flow for an obstacle moving transversely in a rapidly rotating fluid. *Journal of Fluid Mechanics*, **149**, 71-88.
- KILLWORTH, P. D., STAINFORTH, D., WEBB, D. J., PATERSON, S. M., 1989: A free surface Bryan-Cox-Semtner model. Technical Report No. 270, Institute of Ocean Sciences, Deacon Laboratory.
- LONGUET-HIGGINS, M. S., 1969: On the trapping of long-period waves round islands. *Journal of Fluid Mechanics*, **37**, 773-784.
- MCCARTNEY, M. S., 1975: Inertial taylor columns on a  $\beta$ -plane. *Journal of Fluid Mechanics*, **68**, 71-95.
- MESINGER, F., ARAKAWA, A., 1976: Numerical methods used in atmospheric models. *GARP Publication Series*, No. 17, vol. I, 64 p..
- OU, H. W., 1991: Some effects of a seamount on oceanic flows. *Journal of Physical Oceanography*, **21**, 1835-1845.
- SHERWIN, T., DALE, A., 1992: Grid size dependence of the resonant frequency of a submerged cylinder in a stratified ocean. *Ocean Modelling*, **6**.
- SLØRDAL, L. H., MARTINSEN, E. A., BLUMBERG, A. F., 1994: Modelling the response of an idealized coastal ocean to a travelling storm and to flow over bottom topography. *Journal of Physical Oceanography*, **24**, 1689-1705.
- THOMPSON, L. A., 1993: Two-layer quasigeostrophic flow over finite isolated topography. *Journal of Physical Oceanography*, **23**, 1297-1314.
- VERRON, J., LE PROVOST, C., 1985: A numerical study of quasigeostrophic flow over isolated topography. *Journal of Fluid Mechanics*, **154**, 231-252.
- Козлов, В. Ф., 1983: Модели топографических вихрей в океане. Наука, Москва.

# Meereswissenschaftliche Berichte

## MARINE SCIENCE REPORTS

---

- 1 (1990) Postel, Lutz:  
Die Reaktion des Mesozooplanktons, speziell der Biomasse, auf küstennahen Auftrieb vor Westafrika (The mesozooplankton response to coastal upwelling off West Africa with particular regard to biomass)
- 2 (1990) Nehring, Dietwart:  
Die hydrographisch-chemischen Bedingungen in der westlichen und zentralen Ostsee von 1979 bis 1988 – ein Vergleich (Hydrographic and chemical conditions in the western and central Baltic Sea from 1979 to 1988 – a comparison)  
Nehring, Dietwart; Matthäus, Wolfgang:  
Aktuelle Trends hydrographischer und chemischer Parameter in der Ostsee, 1958 – 1989 (Topical trends of hydrographic and chemical parameters in the Baltic Sea, 1958 – 1989)
- 3 (1990) Zahn, Wolfgang:  
Zur numerischen Vorticityanalyse mesoskaliger Strom- und Massfelder im Ozean (On numerical vorticity analysis of mesoscale current and mass fields in the ocean)
- 4 (1992) Lemke, Wolfram; Lange, Dieter; Endler, Rudolf (Eds.):  
Proceedings of the Second Marine Geological Conference – The Baltic, held in Rostock from October 21 to October 26, 1991
- 5 (1993) Endler, Rudolf; Lackschewitz, Klas (Eds.):  
Cruise Report RV "Sonne" Cruise SO82, 1992
- 6 (1993) Kulik, Dmitri A.; Harff, Jan:  
Physicochemical modeling of the Baltic Sea water-sediment column: I. Reference ion association models of normative seawater and of Baltic brackish waters at salinities 1–40 ‰, 1 bar total pressure and 0 to 30°C temperature (system Na–Mg–Ca–K–Sr–Li–Rb–Cl–S–C–Br–F–B–N–Si–P–H–O)
- 7 (1994) Nehring, Dietwart; Matthäus, Wolfgang; Lass, Hans-Ulrich; Nausch, Günther:  
Hydrographisch-chemische Zustandseinschätzung der Ostsee 1993
- 8 (1995) Hagen, Eberhard; John, Hans-Christian:  
Hydrographische Schnitte im Ostrandstromsystem vor Portugal und Marokko 1991 - 1992
- 9 (1995) Nehring, Dietwart; Matthäus, Wolfgang; Lass, Hans Ulrich; Nausch, Günther; Nagel, Klaus:  
Hydrographisch-chemische Zustandseinschätzung der Ostsee 1994  
Seifert, Torsten; Kayser, Bernd:  
A high resolution spherical grid topography of the Baltic Sea
- 10 (1995) Schmidt, Martin:  
Analytical theory and numerical experiments to the forcing of flow at isolated topographic features